

OPTICAL SYSTEM DESIGN OF DIRECT DETECTION SHORT-PULSED  
LASER PROXIMITY SENSOR

A THESIS SUBMITTED TO  
THE GRADUATE SCHOOL OF NATURAL AND APPLIED SCIENCES  
OF  
MIDDLE EAST TECHNICAL UNIVERSITY

BY

EMRAH KORKMAZ

IN PARTIAL FULFILLMENT OF THE REQUIREMENTS  
FOR  
THE DEGREE OF MASTER OF SCIENCE  
IN  
MICRO AND NANOTECHNOLOGY

NOVEMBER 2017



Approval of the Thesis:

**OPTICAL SYSTEM DESIGN OF DIRECT DETECTION SHORT-PULSED  
LASER PROXIMITY SENSOR**

submitted by **EMRAH KORKMAZ** in partial fulfillment of the requirements for the degree of **Master of Science in Micro and Nanotechnology Department, Middle East Technical University** by,

Prof. Dr. Gülbin Dural Ünver  
Dean, Graduate School of **Natural and Applied Sciences**

\_\_\_\_\_

Assoc. Prof. Dr. Burcu Akata  
Head of Department, **Micro and Nanotechnology Dept., METU**

\_\_\_\_\_

Asst. Prof. Dr. Selçuk Yerci  
Supervisor, **Micro and Nanotechnology Dept., METU**

\_\_\_\_\_

Prof. Dr. Şimşek Demir  
Co-Supervisor, **Electrical and Electronics Eng. Dept., METU**

\_\_\_\_\_

**Examining Committee Members:**

Assoc. Prof. Dr. Alpan Bek  
Physics Dept., METU

\_\_\_\_\_

Asst. Prof. Dr. Selçuk Yerci  
Micro and Nanotechnology Dept., METU

\_\_\_\_\_

Assoc. Prof. Dr. Barış Bayram  
Electrical and Electronics Eng. Dept., METU

\_\_\_\_\_

Assoc. Prof. Dr. Mustafa Türkmen  
Electrical and Electronics Eng. Dept., Erciyes University

\_\_\_\_\_

Asst. Prof. Dr. Serdar Kocaman  
Electrical and Electronics Eng. Dept., METU

\_\_\_\_\_

**Date: 09.11.2017**

**I hereby declare that all information in this document has been obtained and presented in accordance with academic rules and ethical conduct. I also declare that, as required by these rules and conduct, I have fully cited and referenced all material and results that are not original to this work.**

Name, Last name: Emrah Korkmaz

Signature :

## **ABSTRACT**

### **OPTICAL SYSTEM DESIGN OF DIRECT DETECTION SHORT-PULSED LASER PROXIMITY SENSOR**

Korkmaz, Emrah

M.Sc., Micro and Nanotechnology

Supervisor : Asst. Prof. Dr. Selçuk Yerci

Co-Supervisor: Prof. Dr. Şimşek Demir

November 2017, 94 pages

In this study, we designed a Laser Proximity Sensor system that measures the distance by analyzing the echo signal reflected from object using time-of-flight principle. The sensor makes a direct-detection using a short-pulsed laser and is capable of detecting objects and measuring distances in a range between 0.5 m and 10 m far from the system. Reflectivities of objects are assumed to lie between 20% and 90% and obeying to Lambertian BSDF (Bi-Directional Scatter Distribution Function). A mathematical model for the laser propagation in the atmosphere was developed. Receiver and transmitter optical system design were performed using a ray tracing software (Zemax). Laser central wavelength was measured for the temperature region of interest (i.e. 0 – 70 °C). A bandpass optical filter was designed to block the background light having a wavelength ranging outside of the laser's emission spectrum at its all operation temperatures. Various signal-processing algorithms were developed to extract the echo signal buried in noise. Finally, laser diode driver, high-speed receiver amplifier and time to digital converter circuit board were designed.

Keywords: Laser Proximity Sensor, Time of Flight, Optical Bandpass Filter, PIN Photodetector, Laser Diode

## ÖZ

### DOĞRUDAN ALGILAMA KISA ATIMLI LAZER YAKLAŞMA SENSÖRÜ OPTİK SİSTEM TASARIMI

Korkmaz, Emrah

Yüksek Lisans, Mikro ve Nanoteknoloji

Tez Yöneticisi : Yrd. Doç. Dr. Selçuk Yerci

Ortak Tez Yöneticisi: Prof. Dr. Şimşek Demir

Kasım 2017, 94 sayfa

Bu çalışmada nesneden yansıyan eko sinyalini uçuş süresi yöntemiyle analiz ederek mesafeyi hesaplayan doğrudan algılama kısa atımlı Lazer Yaklaşma Sensörüne ait sistem tasarımını gerçekleştirdik. Sensör, 0.5 m ve 10 m arasında herhangi bir uzaklıkta bulunan nesnelere kısa darbeli lazer ile doğrudan algılayarak mesafeyi ölçebilmektedir. Nesnelerin yansıtıcılıkları Lambertian çift yönlü saçılma dağılımı fonksiyonu ile (Bi-Directional Scatter Distribution Function, BSDF) %20 ile %90 arasında olduğu varsayıldı. Çalışmada, lazer ışın yayılımının matematiksel modeli geliştirilmiştir. Algılayıcı ve yayınlayıcı birimlerimizin optik sistem tasarımı ışın takibi (Ray Tracing) yazılımı yardımıyla gerçekleştirilmiştir. Lazer merkez dalga boyu ilgilenilen sıcaklık aralığında (0 – 70 °C) ölçülmüştür. Tüm çalışma sıcaklıklarında lazer yayılım spektrumu dışında yer alan dalgaboyuna ait arkaplan ışığını engellemek amacıyla bant geçiren (bandpass) filtre tasarlanmıştır. Gürültü içerisinde gömülü eko sinyalinin tespiti için çeşitli sinyal işleme algoritmaları geliştirilmiştir. Son olarak, diyot lazer sürücü, yüksek hızlı algılayıcı yükselteç ve süre dijital dönüştürücü elektronik devre kartları tasarlanmıştır.

Anahtar Kelimeler: Lazer Yaklaşma Sensörü, Uçuş Süresi, Optik Bant Geçiren Filtre, PIN Fotodetektör, Diyot Lazer

To my family

## ACKNOWLEDGMENTS

I would like to thank to my supervisor Asst. Prof. Dr. Selçuk Yerci and Co-supervisor Prof. Dr. Şimşek Demir for their support, advice and encouragement throughout the research.

I would also like to thank ROKETSAN, Inc. and my Managers, for their support and guidance in my study and letting me use experimental facilities of Laser Systems Design Department.

I would like to thank Umut Bekçi for his help during the laser diode central wavelength measurements and optical bandpass filter design.

I would like to express my deepest gratitude to my wife and parents for their love, support and endless patience.

This study was supported by the Undersecretariat for Defence Industries (SSM) within the scope of Educating Researcher for Defence Industries Programme (SAYP).

## TABLE OF CONTENTS

ABSTRACT .....	v
ÖZ .....	vi
ACKNOWLEDGMENTS .....	viii
TABLE OF CONTENTS .....	ix
LIST OF TABLES .....	xii
LIST OF FIGURES .....	xiii
LIST OF SYMBOLS AND LIST OF ABBREVIATIONS .....	xvi
CHAPTERS	
1. INTRODUCTION .....	1
1.1 Optical Triangulation .....	3
1.2 Phase Change .....	4
1.3 Frequency Modulation .....	5
1.4 Time of Flight .....	7
1.5 Comparison of Distance Measurement Techniques .....	8
1.5.1 Countermeasure .....	8
1.5.2 Target Distance Measurement Accuracy and Response Time .....	9
1.5.3 Cost .....	9
1.6 LPS Power Calculations .....	10
1.6.1 Laser Pulse Modelling .....	10
1.6.2 Energy Intensity on the Target .....	12
1.6.3 Atmospheric Transmission .....	13

1.6.4 Target Surface Reflectivity .....	14
1.6.5 Effective Target Surface Area.....	15
1.6.6 Laser Energy Reflected From Target.....	16
1.6.7 Laser Energy on the Detector.....	17
1.6.8 Number of Photoelectrons Generated in the Detector .....	18
1.6.9 Noise Sources.....	18
1.7 Distance Measurement Algorithms .....	21
1.7.1 Leading Edge Discrimination .....	22
1.7.2 Peak Estimation.....	24
1.7.3 Cross Correlation .....	25
1.7.4 Assessment.....	26
1.8 Example Performance Assessment.....	26
1.9 LPS Conceptual Design .....	29
1.9.1 Transmitter Module.....	29
1.9.3 Receiver Module .....	30
1.9.4 Signal Processing Module.....	32
1.10 LPS Block Diagram .....	32
1.11 Hardware Design .....	35
1.12 Thesis Overview .....	35
2. OPTICAL SYSTEM DESIGN.....	37
2.1 Laser Diode Beam Geometry .....	38
2.2 Transmitter Module Optical Design .....	41
2.3 Receiver Module Optical Design.....	47
2.4 Temperature Dependence of Laser Diode Central Wavelength.....	53

2.5 Interference Bandpass Filter Design.....	55
2.6 Review .....	57
3. MATHEMATICAL MODEL .....	59
3.1 Transmitter Module .....	59
3.2 Receiver Module.....	60
3.2.1 Signal to Noise Ratio .....	62
3.3 Signal Processing Module .....	66
3.3.1 Echo Signal Sampling.....	66
3.3.2 Equivalent In-phase Echo Signal Averaging .....	67
3.3.3 Range Calculation.....	70
3.4 Review .....	75
4. CONCLUSIONS .....	77
APPENDICES	
A. LPS ELECTRONICS .....	79
B. SPLPL90 AND BP104FAS TECHNICAL SPECIFICATIONS .....	87
C. LPS SIMULINK MODEL.....	89
REFERENCES.....	91

## LIST OF TABLES

### TABLES

Table 1.1 Sample system parameters .....	27
Table 1.2 Detector sensitivity wavelength region .....	31
Table 2.1 Merit function calculation results.....	44
Table 2.2 Transmitter lens specifications .....	45
Table 2.3 Optical bandpass filter layer structure.....	56
Table 3.1 LPS Simulink model target range output .....	75
Table B.1 Technical Specifications of Pulsed Laser Diode SPL PL 90 @ 25°C, 100 nsec, 2 KHz [14].....	87
Table B.2 Technical Specifications of PIN Photodetector BP 104 FAS [19].....	87

## LIST OF FIGURES

### FIGURES

Figure 1.1 HDL-64E from Velodyne LIDAR [4] .....	2
Figure 1.2 A schematic of optical triangulation method [adapted from ref.6] .....	3
Figure 1.3 A schematic of phase change method.....	4
Figure 1.4 Frequency modulation technique scheme [adapted from ref.5] .....	6
Figure 1.5 Pulsed time of flight scheme .....	7
Figure 1.6 The power-time plots of the pulse models for the inverse parabolic, square, and Gaussian pulse shapes [adapted from ref.1] .....	12
Figure 1.7 Laser projection area at some distance from the source .....	13
Figure 1.8 Atmospheric transmission spectrum between 1-11 $\mu\text{m}$ [1] .....	14
Figure 1.9 A schematic of detector FOV and collimated laser projection scheme [9] .....	15
Figure 1.10 A schematic showing the target surface modelling when FOV is limiting condition.....	16
Figure 1.11 (a) Specular reflection (b) Lambertian reflection [adapted from ref.1] .....	17
Figure 1.12 Photon counting noise [adapted from ref.1] .....	19
Figure 1.13 Pulsed time of flight method using time to digital converter [8].....	22
Figure 1.14 Leading edge discriminator [adapted from ref.10] .....	23
Figure 1.15 A representation of the leading edge discrimination measurement error [adapted from ref.8] .....	23
Figure 1.16 Peak measurement error due to limited resolution [adapted from ref.10] .....	24
Figure 1.17 Analog peak detector .....	25

Figure 1.18 Cross correlation of a noisy echo signal with a Gaussian reference signal [adapted from ref.10].....	26
Figure 1.19 Probability of detection for a pulse width of (a) 10 ns, (b) 15 ns, (c) 20 ns and (d) 25 ns with respect to various SNR values.....	28
Figure 1.20 SNR variation within the measurement range .....	28
Figure 1.21 The LPS Product Tree.....	29
Figure 1.22 LPS block diagram.....	34
Figure 2.1 Schematic of laser diode elliptical beam geometry (top) and astigmatism (bottom) [13] .....	38
Figure 2.2 Laser diode NS simulation.....	39
Figure 2.3 Laser footprint and radiance in position space .....	41
Figure 2.4 Laser diode modelling using telecentric lens [17] .....	42
Figure 2.5 Laser diode model view in x-z plane .....	44
Figure 2.6 Laser diode model view in y-z plane .....	44
Figure 2.7 Transmitter module optical design (a) y-z plane (b) x-z plane.....	45
Figure 2.8 Laser footprint images on the detector of 100 mm x100 mm dimensions at 1 m, 5 m and 10 m.....	46
Figure 2.9 Laser footprint images on the detector of 100 mm x 100 mm dimensions at 1 m, 5 m and 10 m using LA1951-B as collimation lens .....	47
Figure 2.10 LPS Optical Simulation Model.....	48
Figure 2.11 Power with respect to distance in foggy air .....	50
Figure 2.12 SNR with respect to target distance .....	52
Figure 2.13 Central wavelength shift due to temperature increase .....	54
Figure 2.14 Laser emission spectrum at three different temperatures .....	55
Figure 2.15 Transmission spectrum of the bandpass filter.....	57
Figure 3.1 Simulink model layout of transmitter block .....	60
Figure 3.2 (a) Pulse repetition frequency (b) Gaussian pulse output .....	60
Figure 3.3 Simulink model layout of receiver block.....	61
Figure 3.4 Representative schematic view of TIA .....	62
Figure 3.5 Noise modelling layout.....	64

Figure 3.6 Simulink model output for reference laser signal as well as reflected echo signal with the addition of noise .....	65
Figure 3.7 Detector and preamplifier circuit modelling layout.....	65
Figure 3.8 Two channel ADC operating principle [22] .....	66
Figure 3.9 ADC Model .....	67
Figure 3.10 ADC model output.....	67
Figure 3.11 Averaging module layout .....	69
Figure 3.12 In-phase echo signal averaging for N=1, 3, 10 and 100 .....	70
Figure 3.13 A schematic of delayed cross correlation method [20] .....	73
Figure 3.14 Delayed cross correlation block layout.....	74
Figure A.1 Laser diode driver block diagram .....	80
Figure A.2 Spice simulation of current pulse and start flag.....	80
Figure A.3 3D view of transmitter PCB.....	81
Figure A.4 (a) Signal (Top) layer (b) Ground layer (c) Power layer (d) Signal (Bottom) layer .....	81
Figure A.5 Transmitter layer stack-up .....	82
Figure A.6 Receiver block diagram .....	83
Figure A.7 TIA output and differential signal amplification .....	83
Figure A.8 Bipolar pulses and stop flag signal output .....	84
Figure A.9 3D view of receiver PCB .....	85
Figure A.10 (a) Signal (Top) Layer (b) Ground Layer (c) Power Layer (d) Signal (Bottom) Layer.....	85
Figure A.11 TDC Circuit Schematics .....	86
Figure C.1 The LPS Simulink Model Layout .....	90

## LIST OF SYMBOLS AND LIST OF ABBREVIATIONS

### Symbols

$c$	: Speed of light [m/s]
$E_t$	: Laser pulse energy [J]
$f$	: Focal length [mm]
$h$	: Planck constant [J.s]
$I$	: Laser intensity [ $\text{W}/\text{m}^2$ ]
$k_b$	: Boltzmann constant [J/K]
$n$	: Refraction index
$P_t$	: Laser peak power [W]
$q_e$	: Electron charge [C]
$\theta_t$	: Angular divergence [°]
$\tau_a$	: Atmospheric transmission
$\rho_t$	: Surface reflectivity
$\theta_R$	: Surface reflectance solid angle [sr]
$\eta$	: Detector quantum efficiency
$\nu$	: Frequency [1/s]
$\lambda$	: Wavelength [nm]
$\alpha$	: Atmospheric attenuation coefficient [1/km]

## **Abbreviations**

ADC	: Analog-to-Digital Converter
CCD	: Charged Coupled Device
FAR	: False Alarm Rate
FOV	: Field of View
FPGA	: Field Programmable Gate Array
FWHM	: Full Width Half Maximum
IFOV	: Instantaneous Field of View
LASER	: Light Amplification by Stimulated Emission of Radiation
LIDAR	: Light Detection and Ranging
LPS	: Laser Proximity Sensor
MOSFET	: Metal-Oxide Semiconductor Field-Effect Transistor
NIR	: Near Infrared
PCB	: Printed Circuit Board
PSD	: Position Sensing Device
RADAR	: Radio Detection and Ranging
RMS	: Root Mean Square
SNR	: Signal-to-Noise ratio
SPI	: Serial Peripheral Interface
TDC	: Time-to-Digital Converter
TIA	: Transimpedance Amplifier



## CHAPTER 1

### INTRODUCTION

All remote sensing systems (Radio Detection and Ranging (RADAR), Light Detection and Ranging (LADAR or LIDAR)) essentially measure distance by transmitting electromagnetic energy to objects and then detecting the reflected energy from these objects. The main difference between RADAR, LIDAR and LADAR is the operating frequency band of the utilized electromagnetic energy [1].

Laser Proximity Sensors (LPS) use laser as the electromagnetic energy source and can measure distance more accurately i.e. at a higher resolution than other distance detection systems such as RADAR because of coherent, short wavelength and high directivity of lasers. Furthermore, availability of various wavelengths of lasers and various pulse modulations make LPSs more effective against electro-optic counter measures in many applications [2].

There are numerous LPSs available in the literature for a wide a variety of applications. Their operation principles differ depending on the application requirements. For example, autonomous driving, autonomous flight and 3D mapping applications require high speed measurements for both short (less than 10 m) and long (greater than 100 m) ranges. LPSs utilized in such applications typically operate based on pulsed time of flight method in order to meet requirements mentioned above.

For example, LPS function for autonomous driving is to map and navigate an environment. LPS needs to make thousands of measurements per second in order to generate 3D map of an environment. The LPSs typically use very high speed Analog-to-Digital Converter (ADC) to accomplish that high measurement rate. For instance, HDL-64E from Velodyne LIDAR uses an ADC which operates at 3 GHz to

generate 1 million distance measurements per second. HDL-64E also has 64 pairs of laser diodes and detectors each aligned to provide enough elevation field of view (FOV) and can measure distance up to 120 m [3].



Figure 1.1 HDL-64E from Velodyne LIDAR [4]

The main reason for an LPS design in this work is the absence of relatively low-cost high-speed LPSs for such short distance measurements in the literature. The LPSs available for high speed measurements typically can measure distances greater than 100 m. Thus, they use high power laser diodes, avalanche photodiodes and make use of complex optical design to measure such long distances. All these features make the entire system not so cost-efficient for short distances.

The LPS developed in this work is a miniature LIDAR system. It determines distance between the laser and the surface by measuring the time of flight for a pulsed laser beam. We designed an LPS which is capable of generating up to 10000 distance measurements per second and measuring distances up to 10 m using cost efficient optical and electronics design.

Optical triangulation, phase change, frequency modulation and time of flight are among the most common methods used in LPSs. Distance measured by geometrical means in optical triangulation method is the oldest laser distance sensor technology. Pulsed laser sources are typically used for time of flight method while continuous

laser sources are available for phase difference and frequency modulation methods [5]. Optical triangulation, phase change and time of flight techniques are briefly mentioned in the following sections.

### 1.1 Optical Triangulation

A schematic of optical triangulation method is demonstrated in Figure 1.2. Light from the laser is focused by a lens and forms a laser spot on the target surface. Depending on the position of the image of the laser spot on the detector, the following equation is used to determine the distance [6].

$$R = R_0 - \frac{f \Delta x}{\Delta x \cos(\theta) + d \sin(\theta)} \quad (1)$$

Object distance  $R$  is calculated using the angle between the laser and detector, the focal length of focusing lens and the position of laser spot image on detector.

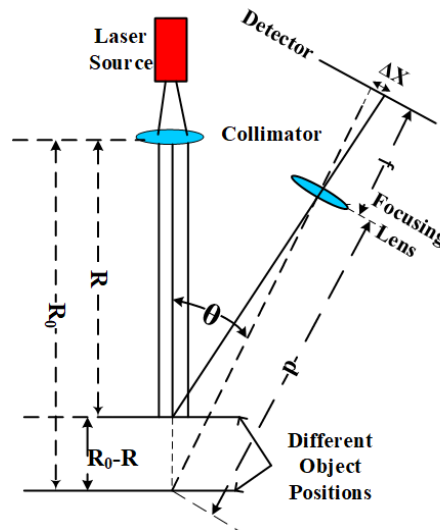


Figure 1.2 A schematic of optical triangulation method [adapted from ref.6]

In optical triangulation method, laser diode and a Charged Coupled Device (CCD) or Position Sensing Device (PSD) is usually used as the detector. The accuracy decreases with distance. Therefore, it is typically used at short distances (less than 10 m).

### 1.2 Phase Change

The distance is calculated using a sinusoidal signal sent to the target. The reflected laser energy is detected on the target and the phase difference between the reference signal and the target is determined. A schematic of the phase change method is given in Figure 1.3.

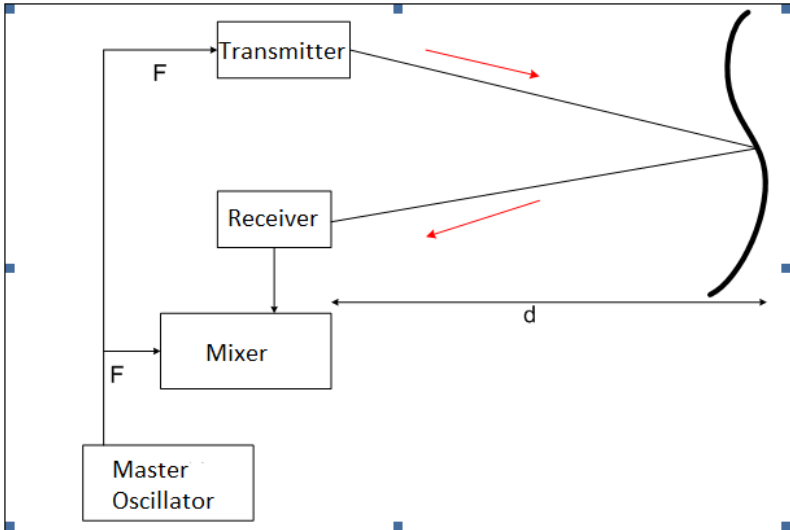


Figure 1.3 A schematic of phase change method

In a system with a modulation frequency  $f_0$ , a target distance of  $d$  and an ambient refraction index of  $n$ , the phase difference can be calculated by the following equation [5].

$$\Delta\phi = \frac{4\pi n f_0 d}{c} \quad (2)$$

The relation between the target distance and the phase difference is expressed by the following equation.

$$d = \frac{c \Delta\phi}{n 4\pi f_0} \quad (3)$$

In phase change technique, distance measurement with an accuracy in the range of mm can be achieved for targets with high surface reflectivity. However, for surfaces with low reflectivity, there is a high degree of performance loss. Due to the correlation of the phase difference measurement accuracy with the signal-to-noise (SNR), phase change method is usually used at distances of several millimeters to 10 m.

### **1.3 Frequency Modulation**

In frequency modulation method, the frequency is measured by using the frequency difference between the frequency modulated signal and the reflected signal from the target. The time-varying frequency graph of the frequency modulation technique is shown in Figure 1.4.

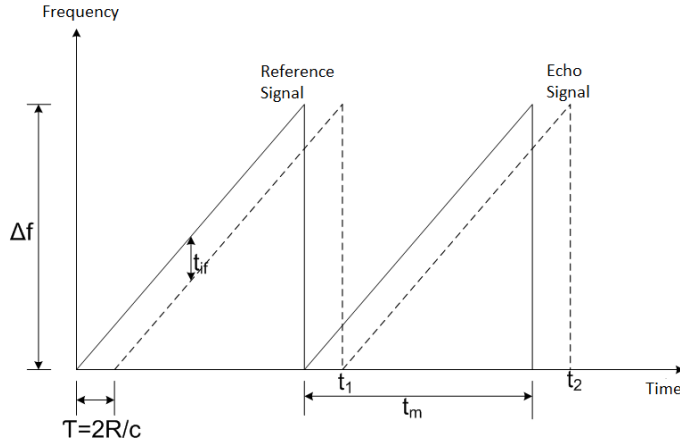


Figure 1.4 Frequency modulation technique scheme [adapted from ref.5]

The reflected signal from the target has the same frequency profile as the reference signal but is displaced by the flight time of the laser as shown by the dashed lines in Figure 1.4.

The reference signal and the reflected signal from the target are then mixed in the "Square Law" diode detector as a frequency difference ( $f_{if}$ ) of the two optical signals. This frequency difference is then measured by a frequency counter.

With the help of a similar triangle rule, the distance to the target is given by the following equation [5].

$$\frac{t_{if}}{\tau} = \frac{\Delta f}{t_m} ; \tau = \frac{t_{if} t_m}{\Delta f} = \frac{2R}{c} \Rightarrow R = \frac{c f_{if} t_m}{2 \Delta f} \quad (4)$$

The frequency modulation method is typically used for short distance measurements (less than 40 m) due to its high dynamic bandwidth and resolution advantages.

## 1.4 Time of Flight

In the time of flight technique or pulsed time of flight, short pulses originated from the laser source are collected by the receiver unit after reflecting from the target surface as shown in Figure 1.5. Thus, the laser pulse travels twice as much as the distance to the target. Since laser travels at the speed of light, the distance to the target can be calculated using the following formula [7].

$$d_{target} = \frac{\Delta t \cdot c}{2} \quad (5)$$

where  $d_{target}$  is the distance between the laser and target,  $\Delta t$  is the total time of flight (travel and return) of the laser pulse, and  $c$  is the speed of light in the medium.

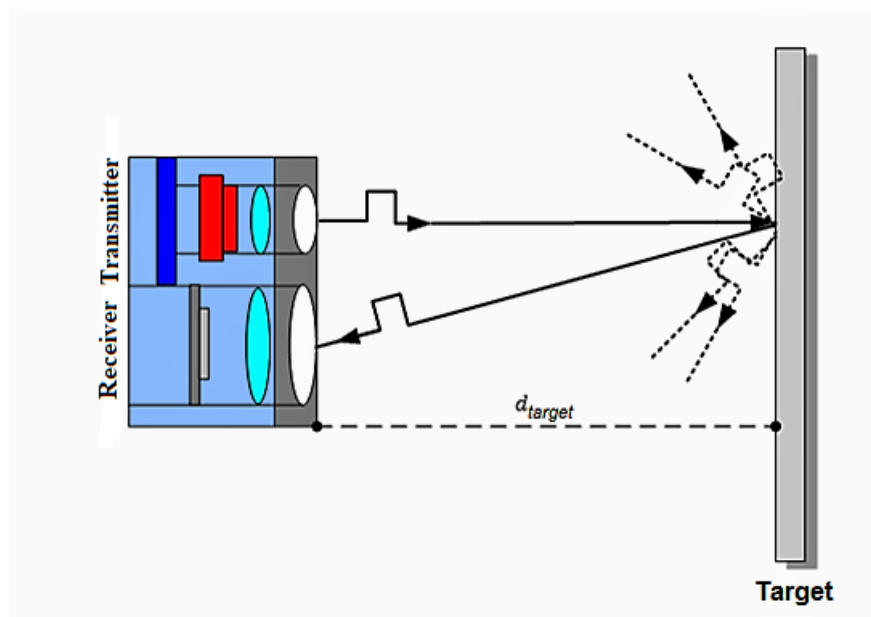


Figure 1.5 Pulsed time of flight scheme

The most important part in the pulsed time of flight method is the time of flight calculation. Light travels in space at about  $\frac{3 \times 10^8 \text{ m}}{\text{s}}$ . Therefore, light travels 30 cm at 1 ns. 1 ns fault that can occur in time of flight measurement is reflected as 15 cm error in distance calculation.

Distance measurement accuracy is directly related to the generation of trigger signals (start / end signals) by the time of flight calculation unit at the right moment. The most common methods used by this unit to generate the relevant trigger signals are "leading edge discriminator", "peak discriminator" and "time correlation". The time between the start and end signals can be measured by a digital counter using analog or digital interpolation methods [2], [8].

Semiconductor laser diodes are usually used as source in the pulsed time of flight method. Laser diodes allow stable, long life and high pulse repetition frequencies. Thus, reliable and fast distance measurements are realized compared to other methods using continuous laser source.

## **1.5 Comparison of Distance Measurement Techniques**

Distance measurement techniques are compared in terms of countermeasure, distance measurement accuracy, response time and cost in the following sections. Due to its high sensitivity and SNR advantages, it has been decided to use the time of flight technique in LPS conceptual design studies.

### **1.5.1 Countermeasure**

Pulse coding techniques used in pulsed laser sources greatly reduce the effectiveness of countermeasures. Nevertheless, the countermeasures for continuous laser sources require more complicated electronics and algorithms. For this reason, techniques using pulsed laser sources (pulsed time of flight and optical triangulation) are more effective in countermeasures than other methods (phase change and frequency modulation technique).

### **1.5.2 Target Distance Measurement Accuracy and Response Time**

When guided ammunition / missile requirements are taken into consideration, it is desirable to measure the distance with accuracy in the range of centimeters between 0.3 and 12 m. All of the above methods can be effectively used at these distances. On the other hand, when the response times are evaluated;

- It is estimated that the response time requirement is not met in the methods using continuous laser source.
- In the optical triangulation method, the accuracy decreases as the distance increases. It is usually used at small distances (less than 10m). For this reason, it is estimated that the distance measurement accuracy requirement at long distances is not met. When using pulsed laser source, the response time is shortened in optical triangulation technique.
- In the phase change method, it is necessary to measure at least two different frequencies in order to make precise distance measurement. This extends the response time duration.
- Response time is similar to phase change method in the frequency modulation method. For the time of flight method, both the fast response times and the accuracy of the measurement can be met. In addition, long distances ( $> 10$  m) can be measured with high accuracy using this method.

### **1.5.3 Cost**

Time of flight and optical triangulation methods are considered to have a lower cost than other mentioned techniques which use continuous laser source cause heating at high powers. Therefore, larger and more complicated cooling block needs to be used in continuous laser sources. In addition, more complex electronic circuitries is used

in the phase shift and frequency modulation techniques compared to the time of flight and optical triangulation method.

## **1.6 LPS Power Calculations**

Range calculations are important both in determining system design parameters and in selecting components. The power on the detector is calculated using the pulse power transmitted by the laser. Range calculations include three steps; the propagation of the laser pulse, reflection from the target surface and detection by the sensor unit.

### **1.6.1 Laser Pulse Modelling**

The power generated by the laser source ( $P_t$ ) determines the shape of the pulse transmitted to the target surface depending on the time. Three commonly used pulse models are square, Gaussian, and inverse parabolic pulse.

#### **1.6.1.1 Square Pulse**

The square pulse is the simplest pulse model. It is a mathematical approach to making an actual laser pulse shape. The time-dependent pulse power is expressed by the following equation [1].

$$P_t(t) = \frac{E_t}{p_w} \times \text{rect}\left(\frac{t}{p_w}\right) \quad (6)$$

The instantaneous time, the pulse energy, the pulse width are denoted by  $t$ ,  $E_t$  and  $p_w$ , respectively. The square pulse is shown in Figure 1.6.

### 1.6.1.2 Gaussian Pulse

Gaussian pulse model is widely used thanks to being the closest to real pulse shape. Gaussian pulse is expressed by the following equation [1].

$$P_t(t) = \frac{E_t}{(\sigma_w \sqrt{2\pi})} e^{-\frac{t^2}{2\sigma_w^2}} \quad (7)$$

Pulse width (Full Width Half Maximum [FWHM]) is denoted by  $\sigma_w$  in units of seconds. The only problem in the Gaussian model is that when the pulse power goes infinitely in the negative direction, it is not zero even if it is very close to zero. This is a contradiction to situation where the actual laser pulse power is zero before firing. However, the time-dependent graph of the measured power after pulse is more accurately expressed by the Gaussian model. Gaussian pulse is shown in Figure 1.6.

### 1.6.1.3 Inverse Parabolic Pulse

The inverse parabolic pulse shape solves the problem of power dissipation in the negative direction in the Gaussian model. The inverse parabolic pulse is expressed by the following equation [1].

$$P_t(t) = \frac{3E_t}{2p_w} \left(1 - \frac{4t^2}{p_w^2}\right) \text{rect}\left(\frac{t}{p_w}\right) \quad (8)$$

In this model, when going to infinity in negative direction, the pulse power is zero. However, the tendency that the actual pulse power shows when it goes to infinity in positive direction is not correctly expressed by this model.

Figure 1.6 shows the square, Gaussian and inverse parabolic models of the laser pulse with energy of 1 Joule and a total pulse width of 6 ns.

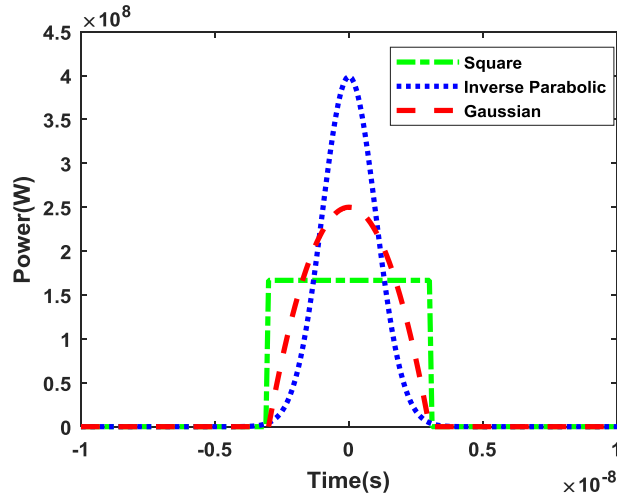


Figure 1.6 The power-time plots of the pulse models for the inverse parabolic, square, and Gaussian pulse shapes [adapted from ref.1]

### 1.6.2 Energy Intensity on the Target

Assuming that the divergence angle of the beam emerging from the laser source is sufficiently small, the area of the projection of the laser on the target is calculated by the following equation [1].

$$S = \pi * \left(\frac{R\theta_t}{2}\right)^2 \quad (9)$$

where  $R$ ,  $\theta_t$  are distance from the source and divergence angle, respectively.

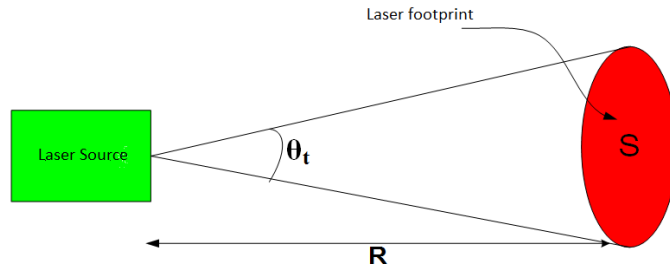


Figure 1.7 Laser projection area at some distance from the source

The laser intensity on target surface with output peak power  $P_t$  is calculated by the following formula.

$$I_{target} \leq \frac{4P_t}{\pi(R\theta_t)^2} \quad (10)$$

As a result of the equation, the intensity is found in units of  $W/m^2$ . Less than or equal symbol is used since laser propagation losses caused by the atmosphere are not accounted for.

### 1.6.3 Atmospheric Transmission

When the light emitted from the laser propagates through the atmosphere, some of the energy is absorbed and scattered by dust, aerosol particles, etc. The amount of loss in energy varies depending on the wavelength of the laser. The atmospheric transmission of the infrared wavelengths is shown in Figure 1.8.

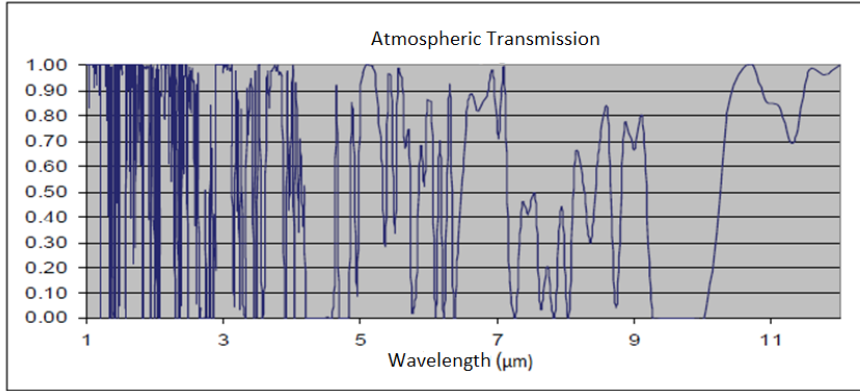


Figure 1.8 Atmospheric transmission spectrum between 1-11 $\mu\text{m}$  [1]

Transmission of light is calculated by the following equation using Beer's law.

$$\tau_a = e^{-\alpha R} \quad (11)$$

where  $\tau_a$  and  $\alpha$  are the atmospheric transmission and the attenuation coefficient, respectively. The energy intensity on the target is expressed by the following equation.

$$I_{target} = \frac{4P_t \tau_a}{\pi(R\theta_t)^2} \quad (12)$$

#### 1.6.4 Target Surface Reflectivity

Target reflectivity is the percentage of the laser beam reflected that fall on the target surface. The surface reflectance coefficient indicated by  $\rho_t$  is a unitless value. Depending on the type of target, the reflectance values typically range from 2% to 80%. The surface reflectivity varies depending on the material and effective target surface area.

### 1.6.5 Effective Target Surface Area

In order to calculate the effective target surface area ( $dA$ ), it is necessary to understand the relation between the FOV of the receiver unit and the angular size ( $\gamma$ ) of the target. As long as the laser projection on the target is not smaller than both parameters, the smaller of these two parameters (FOV and  $\gamma$ ) is used as the target surface area. If the laser beam on the target is smaller than FOV as shown in Figure 1.9, the surface area is equal to the laser projection area.

$$dA = \frac{\pi R^2 \theta_t^2}{4} \quad (13)$$

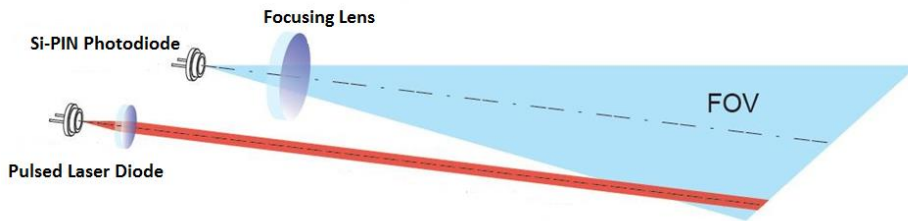


Figure 1.9 A schematic of detector FOV and collimated laser projection scheme [9]

When the FOV is the limiting factor, the detector FOV is modelled as a simple square as in Figure 1.10. The angular size ( $\gamma$ ) of the target is approximately equal to the ratio of size of any side of the square ( $a$ ) to the range to the target ( $R$ ) [1].

The instantaneous field of view (IFOV) of the detector is equal to the ratio of size of the square detector ( $d$ ) to the focal length of focusing lens ( $f$ ) [1].

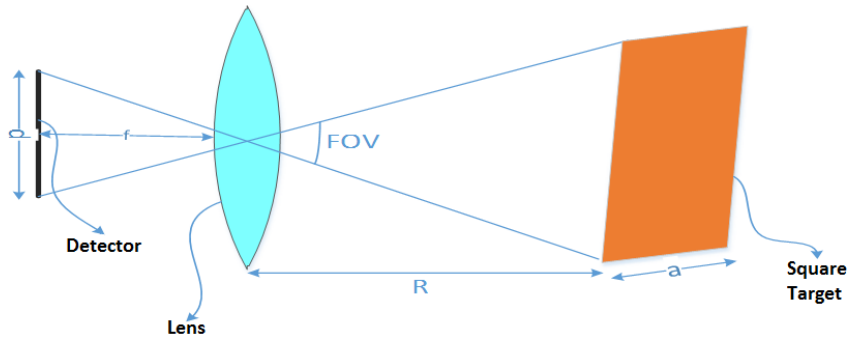


Figure 1.10 A schematic showing the target surface modelling when FOV is limiting condition

As a result, when the angular size of the target ( $\gamma$ ) is smaller than the IFOV of the detector, the effective surface area is the total surface area of the target. If the IFOV is smaller than the target's angular size, then the effective target surface area is given by [1]:

$$dA = \left(\frac{d}{f} R\right)^2 \quad (14)$$

In LPS model, it is assumed that the projection of the laser is always smaller than the target. Therefore, the target effective surface area needs to be expressed by Equation (13).

### 1.6.6 Laser Energy Reflected From Target

After adding the surface reflectance ( $\rho_t$ ) and effective target surface area to the Equation (12), the laser energy ( $P_{ref}$ ) reflected from the target is found by the following equation.

$$P_{ref} = I_{target} \cdot \rho_t \cdot dA \quad (15)$$

There are two different reflection characteristics of surfaces: Specular and Lambertian reflection. On specular surfaces, the angle of incidence and reflection with respect to surface normal are equal to each other. On Lambertian surfaces, light

is assumed to be reflected uniformly to a semi-sphere normal to the surface. In natural surfaces, both specular and diffused reflection occur at the same time. Yet, diffuse reflection typically dominates. In LPS model, we assume that all surfaces show Lambertian reflection characteristics.

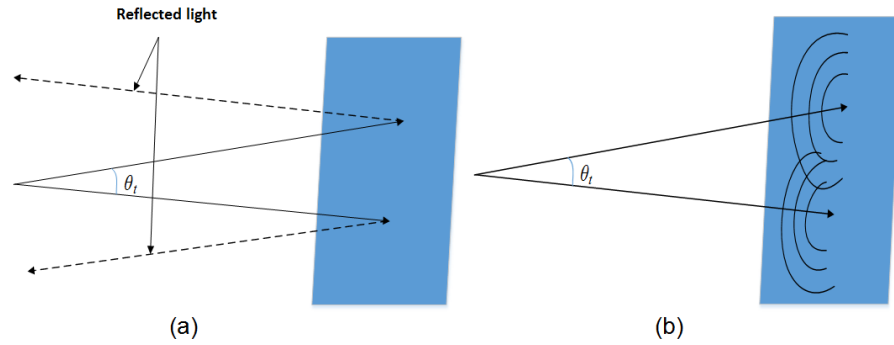


Figure 1.11 (a) Specular reflection (b) Lambertian reflection  
[adapted from ref.1]

### 1.6.7 Laser Energy on the Detector

In the Lambertian reflection, the laser beam reflects at a larger solid angle ( $\theta_R$ ). Therefore, laser intensity reaching the receiver is expressed by the following equation.

$$I_{Rec} = \frac{P_{ref}}{R^2 \theta_R} \tau_a \quad (16)$$

When the sensor input aperture diameter ( $D_R$ ) is added to the process, the laser power incident on the detector is found by the following equation [1].

$$P_{Rec} = \frac{\pi D_R^2 P_{ref} \tau_a}{4R^2 \theta_R} \quad (17)$$

In the LPS model, it is assumed that the laser beam is incident perpendicular to the target surface. The laser beam, which does not fall perpendicular to the target surface, is reflected proportional to the cosine of the incidence angle.

The laser incident on the receiver unit reaches the detector surface after passing through the focusing lens. Laser power incident on the detector surface after adding optical transmission ( $\tau_0$ ) is expressed by the following equation [1].

$$P_{det} = \frac{(\tau_0 \tau_a^2 D_R^2 \rho_t (dA) P_t)}{R^2 \theta_R (\theta_t R)^2} \quad (18)$$

### 1.6.8 Number of Photoelectrons Generated in the Detector

The number of photons produced in the detector is variable and expressed by taking the average. The average number of photons ( $[K]$ ) is calculated by dividing the power incident on the detector throughout the integration period to the energy of each photon [1]. The energy of a photon with frequency ( $\nu$ ) is expressed by Einstein's photoelectric effect theory ( $E = h\nu$ ;  $h$  Planck constant).

$$[K] = \frac{P_{det} \Delta t}{h\nu} \quad (19)$$

The average photoelectron number ( $[N_{signal}]$ ) is then equal to the quantum efficiency of the detector ( $\eta$ ) times the average number of photons incident on the detector.

### 1.6.9 Noise Sources

Many noise sources affect the distance measurements in the LPS. These include noise generated by the system (electronic components, cabling, etc.), statistical

changes created by the light reaching the detector, and stray light (i.e. sunlight). The following noise sources are modelled in this research.

- photon counting noise
- laser speckle
- thermal noise
- background noise

### 1.6.9.1 Photon Counting Noise

The number of photons that the detector counts during the integration period is a variable parameter and its mean value is proportional to expected number of photons. This variability is due to the random arrival time of photons on detector. Therefore, the number of photons in the integration period is uncertain.

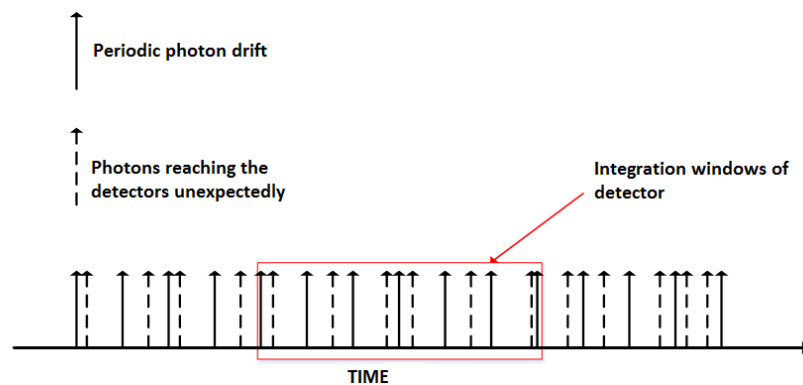


Figure 1.12 Photon counting noise [adapted from ref.1]

This uncertainty in photon counting is expressed by the Poisson distribution [1].

$$\sigma_{fa}^2 = \frac{[N_{signal}]q_e^2}{\Delta t^2} = \frac{2q_e^2 B \eta P_{det}}{h\nu} \quad (20)$$

where the photoconductive variability, electron charge and detector bandwidth are expressed with  $\sigma_{fa}^2$ ,  $q_e$ , and  $B$ , respectively.

### 1.6.9.2 Laser Speckle

Laser speckles are caused by the interference of many coherent laser photons on the detector. This is due to the wave characteristic of the light. It is expressed by the following equation [1].

$$\sigma_{speckle}^2 = [N_{signal}] \left(1 + \frac{[N_{signal}]}{M}\right) \quad (21)$$

In this equation, the variance of the photon current due to the laser speckles is denoted by  $\sigma_{speckle}^2$  and the degree of freedom of light is expressed as  $M$ . Since the laser is coherent,  $M = 1$ .

### 1.6.9.3 Thermal Noise

Detector emits photons due to the black body radiation, which is also a source of noise. The electrical load variation ( $Q_n^2$ ) when an analog / digital converter is connected with the help of any detector capacitance ( $C$ ) is expressed by the following equation [1].

$$Q_n^2 = \frac{k_b T C}{q_e^2} \quad (22)$$

where temperature is shown by  $T$ , Boltzmann constant by  $k_b$ . In general, the capacitance at the detector circuit is unknown. Hence, in practice the thermal noise existing in the detectors is measured by dark current.

#### 1.6.9.4 Background Noise

The background noise is due to signal coming from light sources other than the laser. The sunlight in the FOV of the receiver is the dominating mechanism. These light sources collected by the detector do not carry distance information. However, random arrivals of photons from the background affect the number of photons collected along the integration window. The background noise caused by this change is expressed by the following equation [1].

$$[N_a] = \frac{S_{ay}\Delta_\lambda A_B \rho_t \eta \tau_0 \tau_a D_R^2 \Delta t}{4R^2 h\nu} + N_{ka} \quad (23)$$

Noise due to background, dark current, intensity of background light and electromagnetic bandwidth of narrow bandpass filter are denoted by  $N_a$ ,  $N_{ka}$ ,  $S_{ay}$  and  $\Delta_\lambda$ , respectively.

### 1.7 Distance Measurement Algorithms

The distance is measured using the time between the laser pulse sent towards the target and the echo signal reaching the receiver. As shown in Figure 1.13, the time measurement is carried out with a counter operating at high speed (i.e. gigahertz).

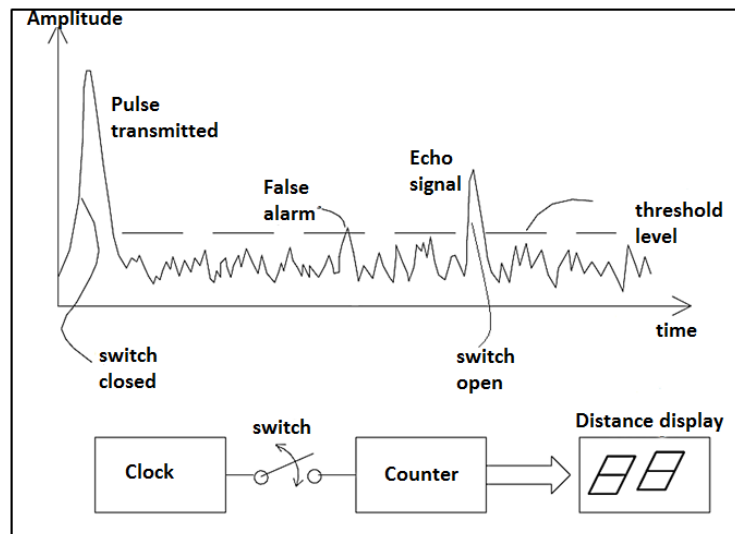


Figure 1.13 Pulsed time of flight method using time to digital converter [8]

The decision to turn on or off the counter at which moment of the transmitted and detected laser pulses directly affects the accuracy of the distance measurement. Therefore, various algorithms need to be used. Three different algorithm techniques are described below.

- Leading edge discrimination
- Peak estimation
- Cross correlation

### 1.7.1 Leading Edge Discrimination

In this method, as shown in Figure 1.14, the point at which the laser pulse passes the predetermined threshold level is found. When the threshold level is reached, the counter starts counting and measures the elapsed time. The counter is deactivated when the return signal exceeds the specified threshold level. The counter outputs the time of flight duration.

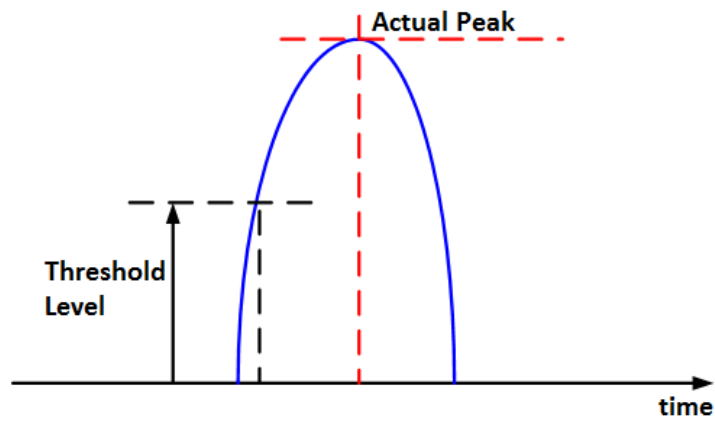


Figure 1.14 Leading edge discriminator [adapted from ref.10]

Although this method is very simple, the pulse amplitude cannot be accurately and precisely measured due to the noise in the environment and the limited counter resolution. The latter one is depicted in Figure 1.15.

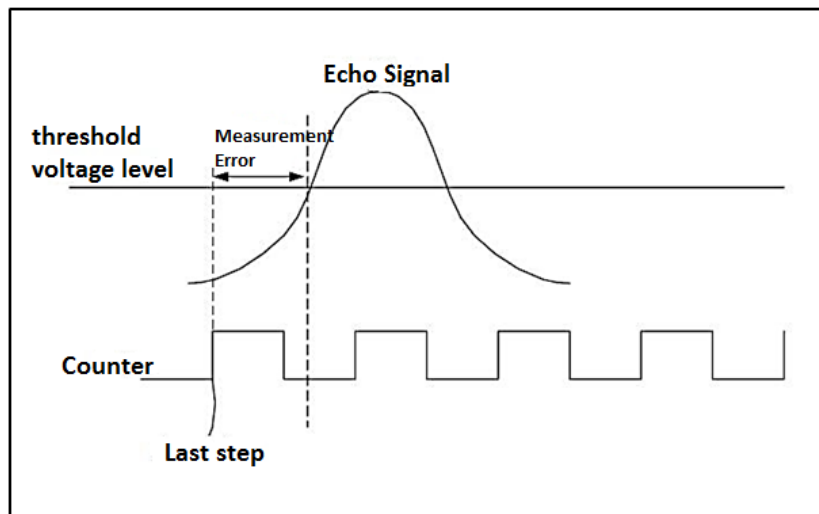


Figure 1.15 A representation of the leading edge discrimination measurement error [adapted from ref.8]

### 1.7.2 Peak Estimation

The peaks of the laser pulses sent to the target and reflected are separately located. The counter runs between both peaks and the time of flight is calculated. Accurate detection of the peak point is directly related to the resolution of the ADC used in the system. Figure 1.16 shows the difference between the actual peak point and the measured peak point due to the limited resolution of the ADC. This problem can be partially reduced by interpolating discrete values. However, interpolation algorithms are typically not optimized for real-time systems.

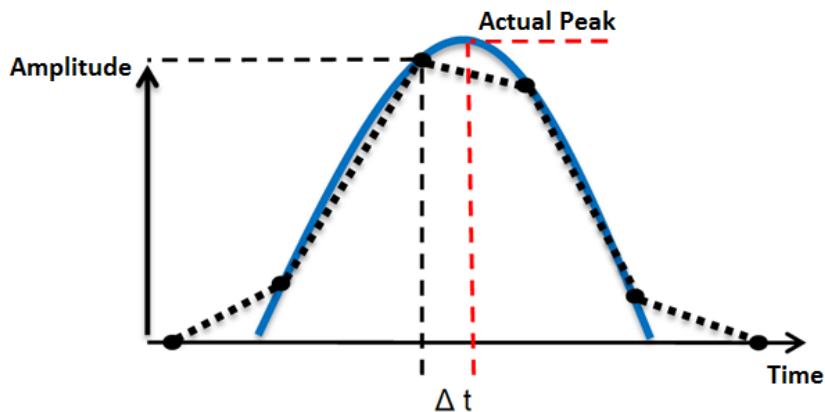


Figure 1.16 Peak measurement error due to limited resolution [adapted from ref.10]

On the other hand, analog peak point of the echo signal can be measured directly with the aid of a comparator. The analog echo signal can be sampled at the peak point using a passive filter.

As shown in Figure 1.17, the analog echo signal crosses zero point irrespective to the pulse amplitude after passing through a high pass filter. The intersection point can be sampled with the aid of a comparator circuit. In this case, the error margin is reduced significantly [11].

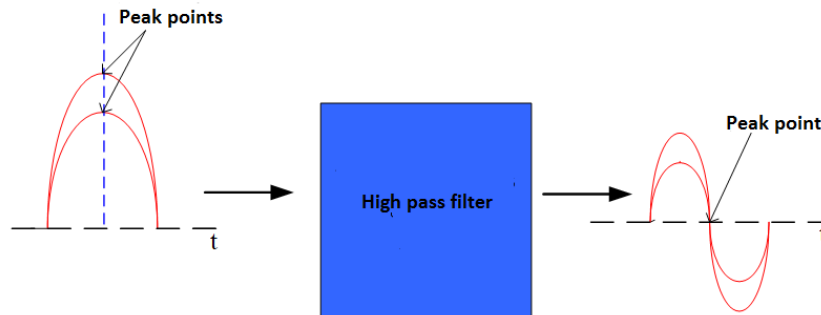


Figure 1.17 Analog peak detector

### 1.7.3 Cross Correlation

In cross correlation, an appropriate reference is determined using one of the pulse models described in Section 1.6.1, cross-correlation is performed between the echo signal and reference signal. The Gaussian pulse model is the most widely used reference model. The echo signal sampled by the ADC is shift registered and stored in memory. Then, when correlated with the reference signal, the highest correlation value gives the peak of the echo signal. With the help of correlation, the noise present in the echo signal is partially eliminated. The cross correlation is mathematically expressed by the following equation.

$$y[n] = \sum_{-\infty}^{\infty} x[k]r[k - n], n = 0, \pm 1, \pm 2, \dots \quad (24)$$

where  $x[k]$  is the input sequence;  $R[k]$  is the reference impulse form and  $y[n]$  is the cross correlation output. In Figure 1.18, it is shown that a noisy echo signal gets smoother after cross-correlation with a Gaussian reference signal. Following cross correlation, the peak point can be measured more precisely.

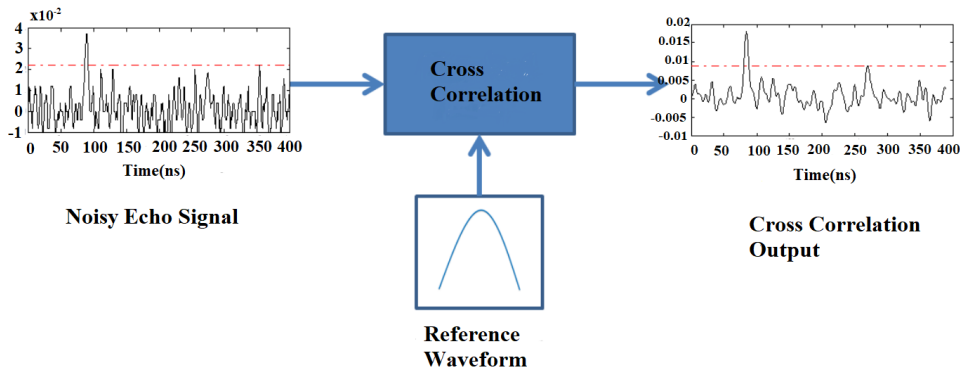


Figure 1.18 Cross correlation of a noisy echo signal with a Gaussian reference signal [adapted from ref.10]

#### 1.7.4 Assessment

When comparing all distance measurement algorithms types, we decided to use the analog peak point calculation method in LPS system design since it allows higher speeds at a lower error rate.

#### 1.8 Example Performance Assessment

Performance analysis was performed on a flat square plate (1m x 1m) target using the following sample parameter values. The parameter values are written taking into account the specifications of the possible components that can be used in the LPS hardware. Calculations were made based on the requirement of 95% detection probability at  $\frac{10^{-4}}{s}$  false alarm rate (FAR) between 0.3-12m.

Table 1.1 Sample system parameters

$P_t$	50W
$\tau_0$	0.6
$\rho_t$	0.15
$D$	0.02m
$R_p$	0.9km
$T$	295K(22°C)
$C$ (Detector capacitance)	1pF
$BW$ (Detector bandwidth)	175MHz
$NEP_{Hz}$ (Noise Equivalent Power of preamplifier)	$\frac{2 \times 10^{-13} W}{\sqrt{Hz}}$ (Si - PIN)
$N$ (Noise factor of the preamplifier)	2
$R_{es}$ (Responsivity of the detector)	$\frac{0.62A}{W}$
$PRF$ (Pulse repetition frequency)	10KHz

Detection probability graphs based on SNR using various false alarm probabilities are given in Figure 1.19. The analysis was repeated according to different laser pulse widths. According to the analysis results, as the FAR decreases, the SNR value required to meet the 95% probability of detection is observed to increase. This shortens the maximum distance that LPS can measure with the probability of 95% detection. For this reason, the maximum range requirement must be taken into account when determining the system level FAR.

According to Figure 1.20, the minimum SNR value required to meet the 95% probability of detection requirement at  $\frac{10^{-4}}{s}$  FAR is approximately 9.5 dB. The SNR change depending on the distance is presented in Figure 1.20. As a result, it is estimated that between 0.3 m and 12 m over these parameter values the required probability of detection and FAR are met.

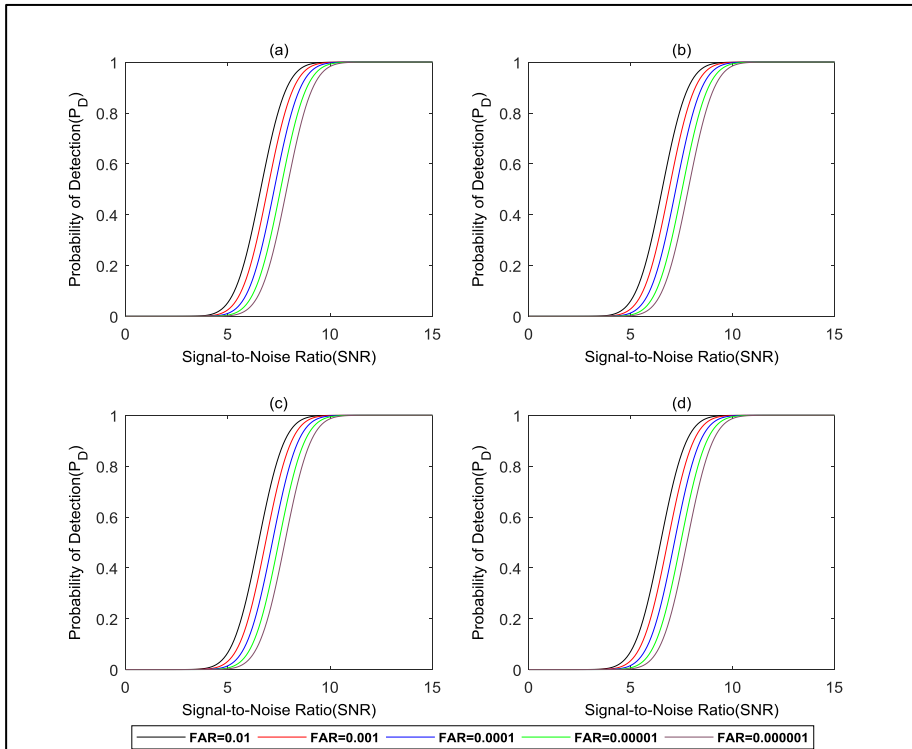


Figure 1.19 Probability of detection for a pulse width of (a) 10 ns, (b) 15 ns, (c) 20 ns and (d) 25 ns with respect to various SNR values

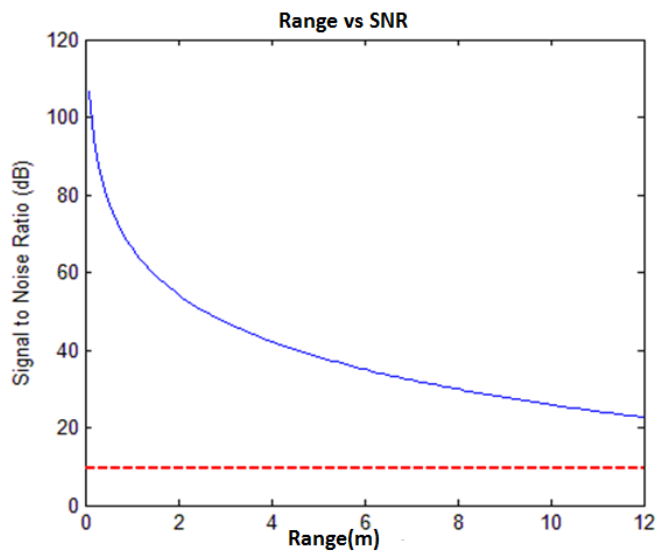


Figure 1.20 SNR variation within the measurement range

## 1.9 LPS Conceptual Design

As shown in Figure 1.21, the LPS consist of 3 basic modules and a mechanical body in which the modules are placed.

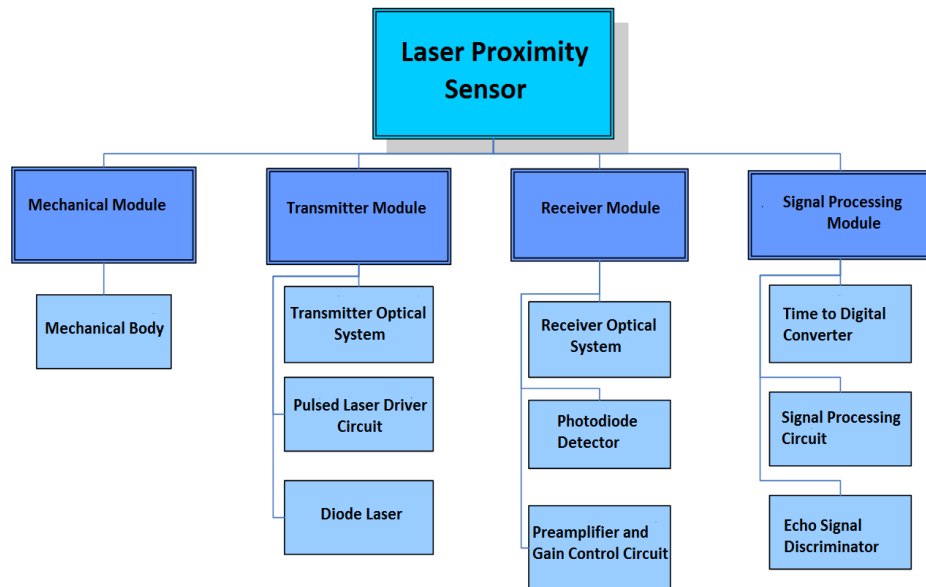


Figure 1.21 The LPS Product Tree

### 1.9.1 Transmitter Module

The basic parameters that determine the performance of LPS are the transmitted peak power, pulse width, pulse rise time and pulse repetition frequency. The amount of the required power varies from a few watts to several kilowatts depending on the application area and range requirement.

The factors determining the power requirement of the laser can be listed as follows.

- Range requirements
- Target type (automobile, bicycle tire, aircraft, etc.)
- Target cross-sectional area,
- Visibility

- Detector sensitivity (response time, quantum efficiency, etc.)

While laser pulse width affects the distance measurement resolution, pulse rise time affects the distance measurement accuracy. Typical pulse widths vary from 2 to 100 ns depending on the resolution requirements of LPS used for anti-tank and air targets. Depending on the requirement for distance measurement accuracy, the pulse rise time varies from 1 to 30 ns.

The pulse repetition frequency requirement is determined by the required SNR and FAR values. The SNR is improved by increasing the amount of pulses integrated in the unit. Number of required pulses for integration determines the pulse repetition frequency. The required pulse repetition frequency for LPS ranges from 10 to 100 kHz.

The amount of power required for LPS applications is generally up to 100W. This is easily met by high-power pulse laser diodes. Microchips solid state lasers are ideal for higher power requirements. Due to cost-effective and compactness features, it is envisaged to use high-power pulsed laser diode in LPS design. The detector used determines the wavelength selection of the laser source. In LPS applications, near infrared region is generally selected. In the LPS design, the sensitivity of the silicon detector was examined and we decided to use a 905 nm laser.

The laser diode driver circuit in the transmitter module controls the pulse repetition frequency, pulse width and peak power. In addition, since the divergence of laser diode is high, a focusing lens is used.

### **1.9.3 Receiver Module**

The most critical component in the receiver module is the detector. The receiver module parameters affecting LPS performance are described below.

- Detector sensitivity
- Detector bandwidth
- Amplifier gain

### 1.9.3.1 Detector Sensitivity

The most effective parameter to determine the sensitivity of the detector is the SNR. The SNR is derived from the FAR value. The detector sensitivity requirement also determines what kind of detector to use. The most widely used detectors in LPS applications are PIN and avalanche photodetectors. Avalanche photodetectors have higher sensitivity than PIN detectors. However, this also applies to noise levels. Depending on the detector material, the wavelength range they are sensitive to is shown in Table 1.2.

Table 1.2 Detector sensitivity wavelength region

Detector type	Material	Wavelength(nm)
Semiconductor	Silicon	400-1000
Semiconductor	Germanium	600-1800
Semiconductor	Indium arsenide	1500-3000
Semiconductor	Lead sulfide	1500-3300
Semiconductor	Lead selenide	1500-6000

It is considered to use silicon detector in LPS design because of their low cost and low detector noise level. Germanium detectors were not included in the design because of the high noise ratios.

### 1.9.3.2 Detector Bandwidth

Bandwidth (BW) requirement is expressed by the following equation. It depends on the rise time ( $t_r$ ) of the laser pulse. Bandwidth is typically represented in units of (MHz/ns) .

$$BW = \frac{350MHz}{t_r} \quad (25)$$

### 1.9.3.3 Amplifier Gain

Amplifier gain is a parameter that affects the voltage output and minimum SNR required to generate the start and end signals used in range calculations.

### 1.9.4 Signal Processing Module

The signal processing module consists of a timing discriminator that generates start and end signals, a time to digital converter that measures the time of flight and a digital signal processing unit that runs specific signal processing algorithms and calculates distance information. Accordingly, the differential echo signals generated by the receiver module pass through the high frequency pass filter. With the help of the comparator, the echo signal is separated from the noise and the end signal is generated. The start signal ( $t_0$ ) is generated by the transmitter module. Both signals are transmitted to the time to digital converter circuit in the signal processing unit to calculate the time of flight for the pulse. With the help of microprocessor, distance information is calculated by running specific signal processing algorithms.

### 1.10 LPS Block Diagram

The flow chart of the LPS system operation is presented in Figure 1.22. The laser diode controlled by the drive circuitry forms the laser signal at the desired pulse width and repetition frequency. Laser signal is then redirected to the target with the aid of a lens. Meanwhile, the laser driver circuit sends the start signal tag to the time

to digital converter. The reflected laser signal from the target is focused onto the detector with the focusing lens. The current output of the detector is converted to voltage output by the transimpedance amplifier (TIA) circuit. The voltage output is then amplified by the post-amplifier circuit and sent to the signal processing unit. The signal peak point is sampled with the aid of a high frequency pass filter. If the sampled peak exceeds the required minimum SNR value, it sends an end signal tag to time to digital converter. Time of flight information is sent to the microprocessor after the time between the start and end signal tags have been calculated by time to digital converter. Distance information is calculated with the aid of digital signal processing algorithms running on the microprocessor. The connections in the block diagram are shown as representations. It does not represent actual electrical connections.

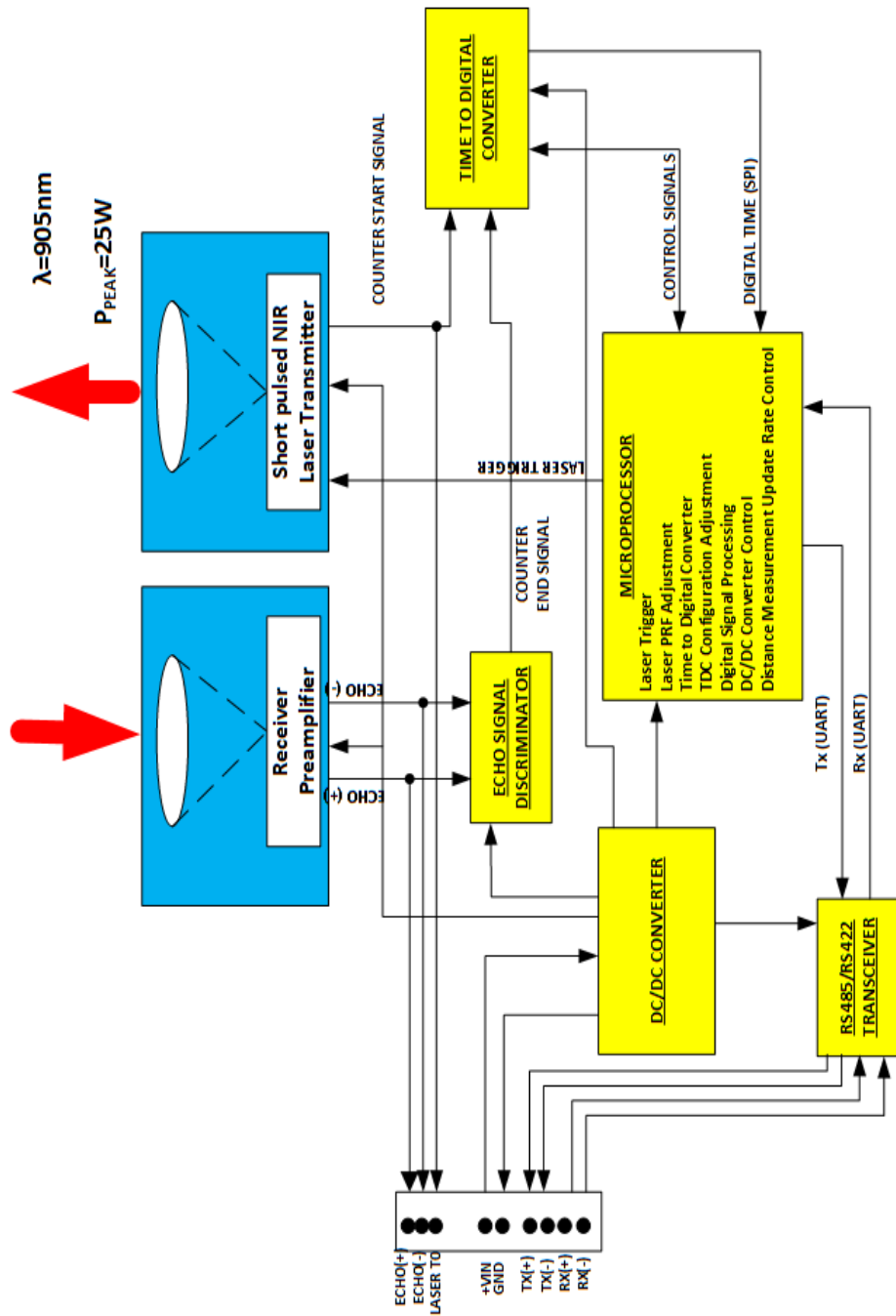


Figure 1.22 LPS block diagram

## **1.11 Hardware Design**

The developed LPS consists of 3 separate printed circuit boards (PCB), two lenses and a mechanical body. LPS electronics design details which include transmitter and receiver circuit simulations as well as PCB layout studies are given in Appendix A.

## **1.12 Thesis Overview**

The LPS developed in this work operates based on pulsed time of flight principle and measures distances between 0.5 m and 10 m.

Chapter 1 discusses basic principles of various distance measurement systems as well as laser power calculations.

Optical design details are discussed in chapter 2 in terms of transmitter and receiver lens design along with an optical bandpass filter design. In addition, optical performance analysis results are presented.

A mathematical model of the LPS is described in chapter 3 using various signal processing algorithms to increase SNR.

Conclusions are given in chapter 4.



## CHAPTER 2

### OPTICAL SYSTEM DESIGN

In order for LPS to perform target detection and distance measurement, the laser must be directed to the target with minimal energy loss. Therefore, laser light needs to be collimated. Similarly, the reflected light should be collected by the detector efficiently. With the help of optical components (lens, mirror etc.), the laser with small divergence angles is directed onto the target and the reflected light is collected on the detector.

Special optical design is required depending on requirements derived by laser beam geometry, detector dimensions and distance etc. Custom design optical components are often used to meet the system requirements even though off-the-shelf optical components may reduce cost. Thus, the design and analysis studies of the optical components to be used in LPS were made using Zemax [12]. Zemax performs ray tracing in two different ways so called 'sequential' and 'non-sequential (NS)' mode. In sequential mode, ray tracing sequence is defined by the user by specifying the order of surfaces. In non-sequential mode, ray tracing is irrespective to the surface ordering. Therefore, sequential mode has a higher processing speed. Non-sequential mode is typically used for analysis work such as stray light. The design work described in this research was made using sequential mode due to the speed and the efficiency of the optimization. On the other hand, simulation and analysis studies were carried out in the non-sequential mode.

## 2.1 Laser Diode Beam Geometry

Laser diode was used as source in our LPS design. Semiconductor laser diode is preferred because of its low cost, small volume, ability to choose different wavelengths, and high pulse repetition frequency. However, laser diodes have astigmatism and elliptical beam geometry as shown in Figure 2.1. Therefore, laser diode beam needs to be shaped by the optical system according to system requirements when it is used in LPS applications.

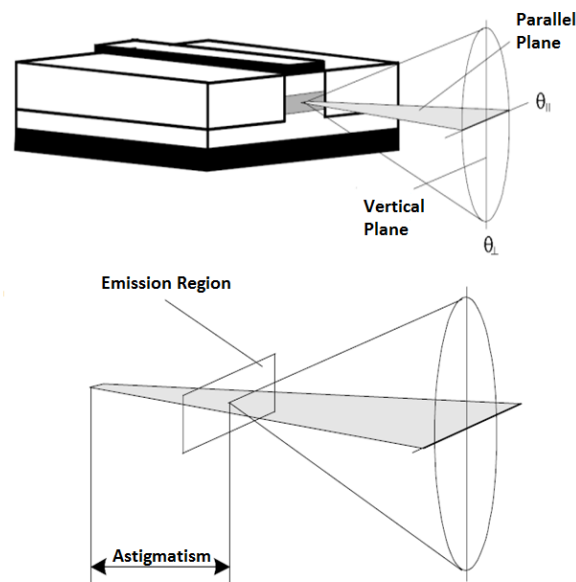


Figure 2.1 Schematic of laser diode elliptical beam geometry (top) and astigmatism (bottom) [13]

The laser diode used in LPS design is SPLPL90 produced by OSRAM [14]. Detailed technical specifications of the laser diode with high power and short pulse width characteristics are given in Appendix B.

Zemax simulation of the laser diode (SPLPL90) with divergence angles  $\theta_{\parallel} = 9^{\circ}$  and  $\theta_{\perp} = 25^{\circ}$ , peak power of 25 W is shown in Figure 2.2. Divergence angles are

usually given by laser diode manufacturers at full width half maximum (FWHM). Zemax uses the Gaussian intensity profile to define the half width at  $1/e^2$ . In  $TEM_{00}$  mode, there is a linear relationship between these two values for a symmetric and normalized Gaussian light [15].

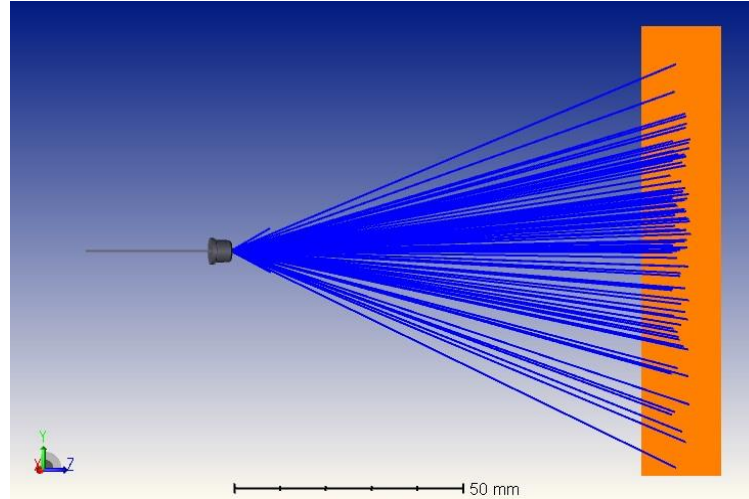


Figure 2.2 Laser diode NS simulation

Gaussian beam intensity is determined by the following equation [15].

$$I = I_0 e^{-\frac{2r^2}{w^2}} \quad (26)$$

where  $w$ ,  $r$  and  $I_0$  are the half-width of light at  $1/e^2$ , the radial distance from the beam center and peak intensity, respectively. The width of the light in a given  $z$  position is [15];

$$w(z) = w_0 \left[ 1 + \left( \frac{\lambda z}{\pi w_0^2} \right)^2 \right]^{\frac{1}{2}} \quad (27)$$

where  $w_0$  is the beam waist radius at  $1/e^2$ .

For a normalized Gaussian beam, FWHM is the width at the half of the peak.

$$0.5 = e^{-\frac{2r^2}{w^2}} \quad (28)$$

If  $r$  is replaced by  $FWHM/2$ ;

$$0.5 = e^{-\frac{2\left(\frac{FWHM}{2}\right)^2}{w^2}} \quad (29)$$

After taking logarithm and simplified, the following linear equation is obtained.

$$w = 0.85 * FWHM \quad (30)$$

The simulation is performed by calculating the corresponding values of these angles for the Gaussian beam using the following equation.

$$\alpha_x = (0.85)\theta_{fwhm} \quad (31)$$

According to the equations above, the new divergence angles are  $\alpha_x = 7.65^\circ$  and  $\alpha_y = 21.25^\circ$ . The simulation includes the signal of the detector at a distance of 100 mm from the laser diode.

According to the simulation, the angular radiance in x and y axes are given in Figure 2.3.

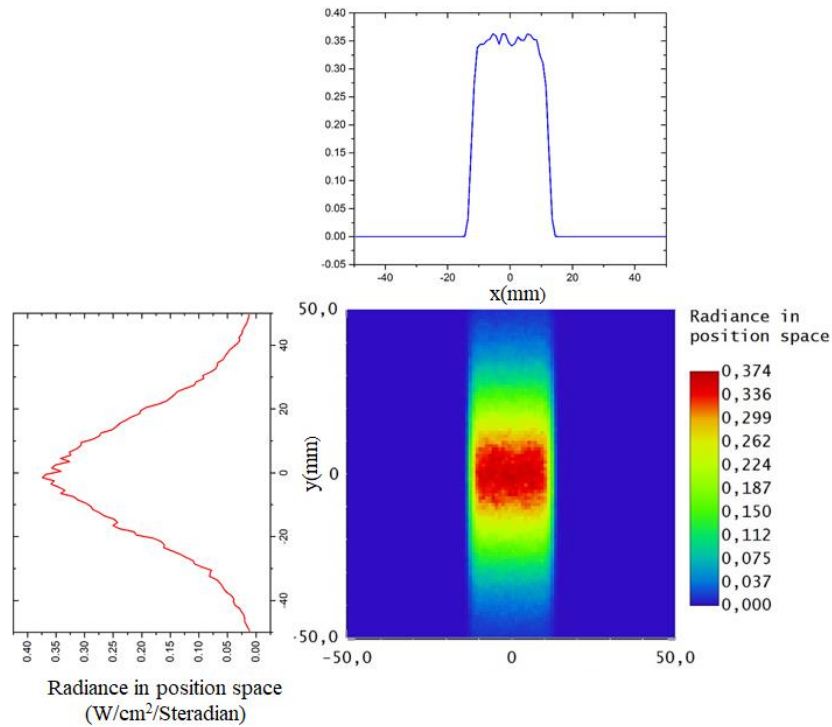


Figure 2.3 Laser footprint and radiance in position space

## 2.2 Transmitter Module Optical Design

Wide and different divergence angles of laser diode beam have to be collimated in both axes using a lens or lenses. Due to the astigmatic light characteristic it is not possible to simulate a direct laser diode source in the Zemax's sequential mode. Therefore, two different methods are used below in order to simulate the astigmatic light source.

### Method I

Divergence angle in y axis is defined as 'object space NA' in sequential mode.

$$NA_y = \sin(\theta_y) = \sin(21.25) = 0.36 \quad (32)$$

Vignetting is then defined on the x-axis to obtain a parallel divergence angle. Using the vignetting value VCX parameter, the  $NA_x$  value is calculated by the following equation.

$$NA_x = NA_y(1 - VCX) = \sin(\theta_x) = 0.13 \Rightarrow VCX = 0.64 \quad (33)$$

In Zemax merit function editor window, the divergence angles can be controlled using the RAID function.

### **Method II**

Although the astigmatic divergence angles are obtained in the first method, the aperture that the laser diode emits is not modelled. This causes erroneous results in laser diodes with large chip size.

In this method, the light coming from an infinite at a certain angle focuses on the telecentric lens through the aperture in the front focus [16].

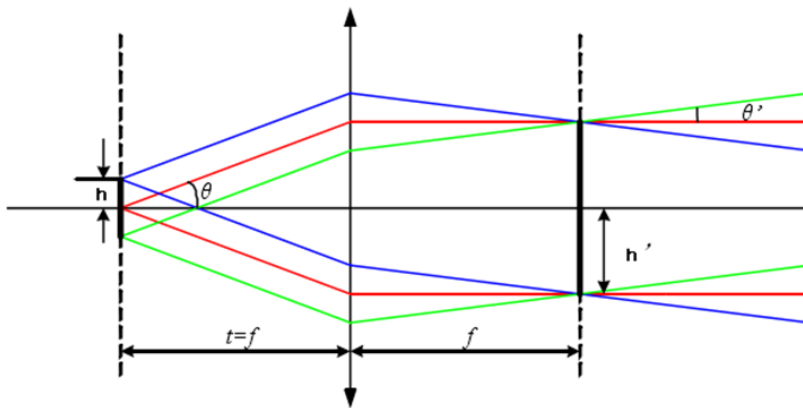


Figure 2.4 Laser diode modelling using telecentric lens [17]

As shown in Figure 2.4, the image dimensions ( $h'$ ) formed in the back focal plane of the telecentric lens is the laser diode chip size and  $\theta'$  is the divergence angle.

Image dimensions and angles are calculated using  $h' = f \tan \theta$  where  $f$  is the focal length of the telecentric lens and  $\theta$  is the angle of incidence coming from infinite. By using the different arrival angles defined in the X and Y plane, the chip dimensions of the laser diode can be modelled.

Laser diode divergence angles are modelled using  $\tan \theta' = hf$  where  $h$  represents the dimensions of the stop surface at the X and Y axes in the optical input aperture, and  $\theta'$  represents the divergence angle of the laser diode. With this method, divergence angles and chip dimensions on the X and Y axes of the laser diode can be accurately modelled.

Telecentric lens is modelled using paraxial surface. Other parameters have been calculated with the help of the above equations. For the laser diode planned to be used in LPS, the following lens parameters are identified.

$$h'_x = 0.1 \text{ mm}, h'_y = 0.001 \text{ mm}, f = 1 \text{ mm} \Rightarrow \theta_x = 5.7106^\circ, \theta_y = 0.0573^\circ, h_x = 0.1343 \text{ mm}, h_y = 0.3889 \text{ mm}$$

The Zemax 3D layout images of the laser diode model are given in Figure 2.5 and Figure 2.6. The model can also be verified by checking laser diode chip dimensions and divergence angles with the help of Zemax merit function operators. The incidence angle on the image plane is calculated using the RAID operator, and the chip dimensions are calculated using the REAX and REAY operators. Zemax uses these operators to calculate the coordinates (REAX and REAY) and the angles (RAID) of the light on any surface passing through the center of the entrance aperture (chief ray) and the edge (marginal ray).

The calculation results of the Merit function is given in Table 2.1. According to the values in the last column, the correctness of the model can be verified.

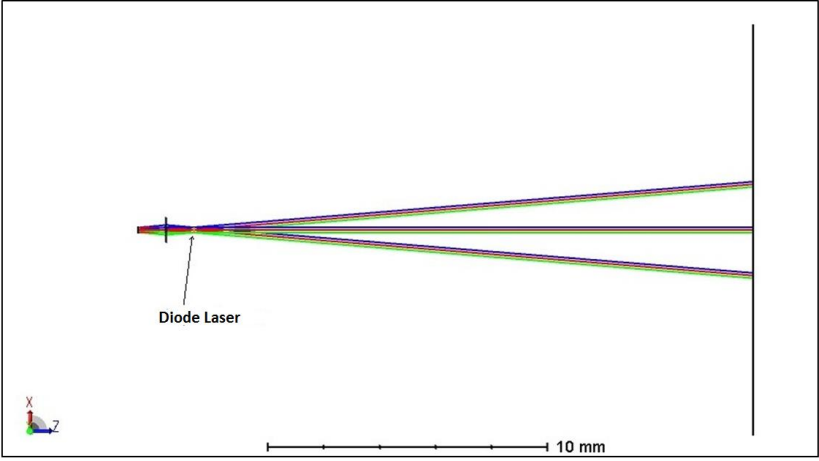


Figure 2.5 Laser diode model view in x-z plane

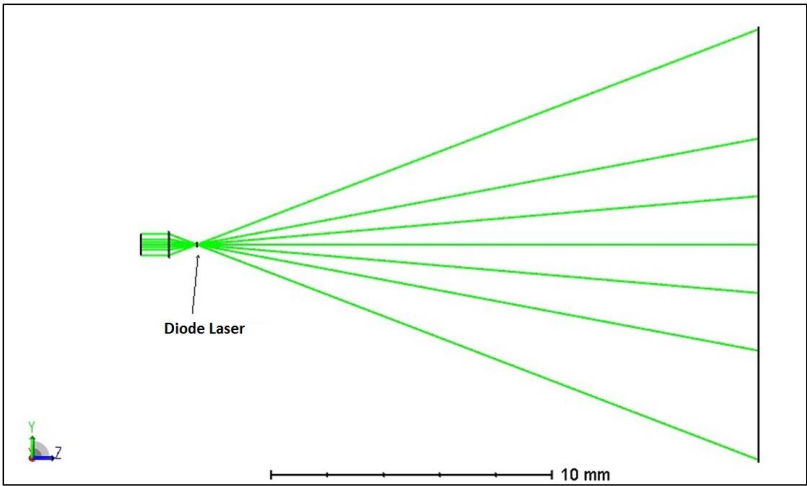


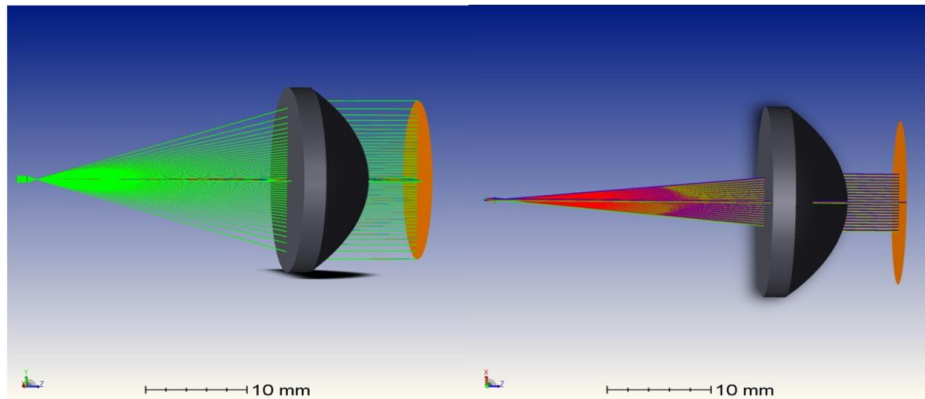
Figure 2.6 Laser diode model view in y-z plane

Table 2.1 Merit function calculation results

Num	Type	Int1	Int2	Hx	Hy	Px	Py	Target	Value
1	REAX	3	1	1	0	1	0	0.00E+00	1.00E-01
2	REAY	3	1	0	1	0	1	0.00E+00	1.00E-03
3	RAID	4	1	0	0	0	1	0.00E+00	2.13E+01
4	RAID	4	1	1	0	0.344	0	0.00E+00	7.62E+00

In the optical design of the transmitter module, the laser diode is modelled using the second method described above. It is planned to use a plastic aspheric lens or lenses for low cost and production advantages in LPS system design. Due to the astigmatic characteristic of the laser diode, it is not possible to generate a circular beam by minimizing the divergence angles of each of the two axes using a single lens. However, an elliptical projection will be obtained. Since the laser footprint shape is important only in terms of the target dimensions to be detected, it is considered that the LPS performance will not be affected up to 10 m due to elliptical beam shape.

Zemax design was optimized with the 'spot angular radius' criterion in merit function because of afocal system design. Zemax 3D layout images are given in Figure 2.7.



(a)

(b)

Figure 2.7 Transmitter module optical design (a) y-z plane (b) x-z plane

Lens specifications are given in Table 2.2.

Table 2.2 Transmitter lens specifications

Lens type	Plano-Convex
Diameter	25 mm
Curvature radius	14.687 mm
Center thickness	8 mm
Material	Acrylic
Conic constant	-0.579
Effective focal length	30.347 mm

The following values were obtained using the RAID operator for the angle of the laser diode with respect to the surface normal of image surface in the x and y axis.

$$\theta_x = 0.185^\circ, \quad \theta_y = 0.013^\circ$$

Because the divergence angle on the x axis is higher, the x-axis expansion in the laser footprint is larger as the distance increases.

The spatial energy distribution on the detector at various distances from laser diode is given in Figure 2.8. Detector images also provide information about laser footprint.

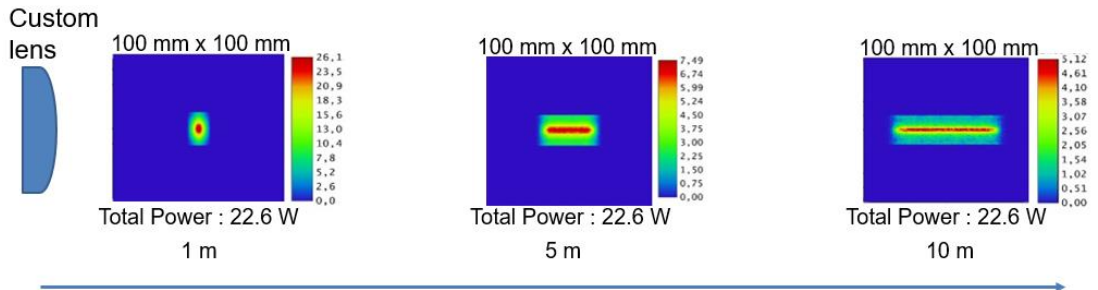


Figure 2.8 Laser footprint images on the detector of 100 mm x100 mm dimensions at 1 m, 5 m and 10 m

Off-the-shelf lens from Thorlabs was also used in Zemax simulation in order to compare custom lens design collimation performance with a COTS lens. LA1951-B from Thorlabs was selected due to its similar optical properties such as focal length, diameter and type [18]. LA1951-B is a plano-convex lens and has a focal length of 25.4 mm. It has an anti-reflective coating for wavelengths between 650 nm and 1050 nm. The spatial energy distribution on the detector at various distances from laser diode using LA1951-B as collimation lens is given in Figure 2.9.

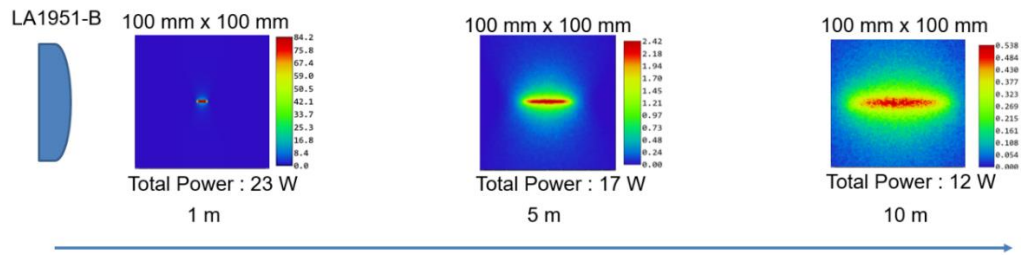


Figure 2.9 Laser footprint images on the detector of 100 mm x 100 mm dimensions at 1 m, 5 m and 10 m using LA1951-B as collimation lens

Laser footprint sizes at various distances shown in Figure 2.9 are similar to the ones shown in Figure 2.8. However, total power incident on detector shows that custom lens design collimates much more rays thereby increasing the total power at long distances with the same size detector than LA1951-B.

### 2.3 Receiver Module Optical Design

One of the most important factors in the optical design of the receiver module is the detector size. We decided to use BP104FAS detector model produced by OSRAM firm in our LPS design [19]. Technical specifications of BP104FAS are given in Appendix B. Other factors that affect LPS performance are lens diameter and focal length. The amount of light collected is proportional to square of the receiver lens diameter. This relation is shown on Equation (17). Therefore, this affects the longest distance that can be measured depending on the lens diameter. The focus distance affects the FOV along with the size of the detector. The receiver lens is only able to collect the light reflected from objects that are in its FOV. Since LPS distance requirements are between 0.5 m and 10 m, a minimum of 25 mm diameter conical plano-convex lens is needed. Thus, we decided to use the same lens designed for the transmitter module in the receiver module.

Initially, FOV was calculated based on effective focal length of the lens designed for transmitter module ( $\sim 30\text{mm}$ ) and detector size ( $2.2\text{ mm} \times 2.2\text{ mm}$ ).

$$\text{Field of View (FOV)} = 2 * \arctan\left(\frac{1.1}{30}\right) = 4.2^\circ \quad (34)$$

Although the FOV is quite small, it is estimated that a new lens design of the same diameter contributes to performance less than the cost increase. Any lens design with an  $F$  number less than 1 is both difficult to manufacture and very costly. On the other hand, because the reflection characteristics of the most targets in nature are Lambertian, the detector collects light from target even from very close distances.

Laser diode, receiver/transmitter module lenses and detector are modelled in the Zemax non-sequential mode as shown in Figure 2.10.

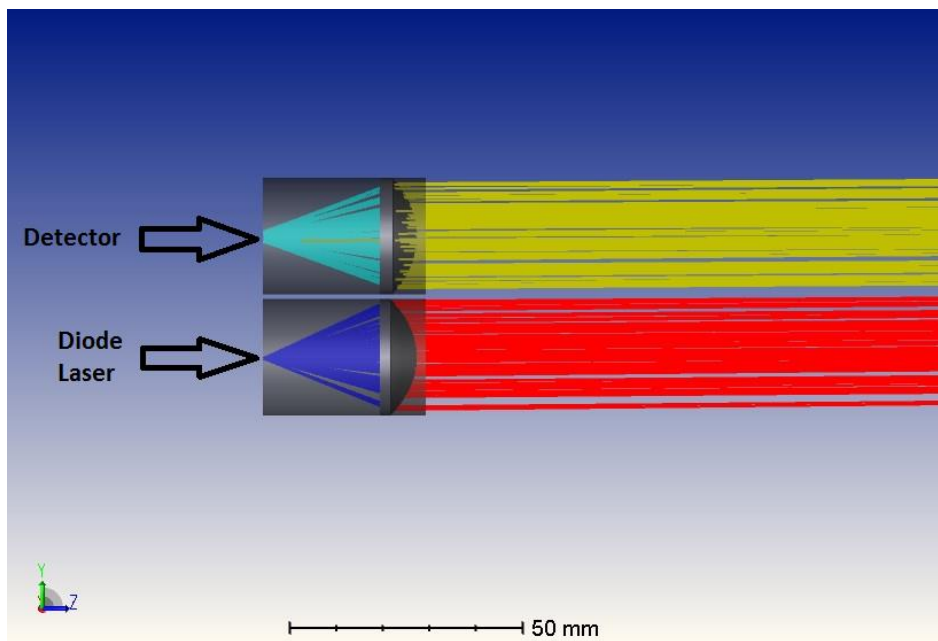


Figure 2.10 LPS Optical Simulation Model

Because atmospheric transmission is not taken into account in the Zemax simulations, the analysis was performed under foggy conditions to represent harsh environment.

Atmospheric attenuation constant is calculated using the following equation [20].

$$\alpha = \frac{3.91}{R_v} \left( \frac{\lambda}{0.55} \right)^{-q} \quad (35)$$

$R_v$ : visibility (km)

$\lambda$  : laser wavelength ( $\mu\text{m}$ )

$q$  : size distribution of scattered particles

$q = 1.6$           high visibility ( $R_v > 50$  km)

$= 1.3$           average visibility ( $6 \text{ km} < R_v < 50$  km)

$= 0.585 \times R_v^{\frac{1}{3}}$  low visibility

The simulation was performed using a flat surface target with dimensions of 0.5 m x 0.5 m and 20% reflectivity at 905 nm wavelength. Target reflectivity is modelled as Lambertian. Moving the target distance from 0.1 m to 10 m, the amount of power incident on the detector is calculated. Zemax is configured to trace one million rays in order to increase the simulation accuracy.

The simulation was repeated by positioning the target at an angle of  $0^\circ$  and  $45^\circ$  relative to the LPS axis. The results obtained are shown in Figure 2.11.

As shown in Figure 2.11, the amount of power incident on the detector at very close distances (10-40 cm) drops considerably. In LPS optical design, parallelism of the optical axes of the transmitter and the receiver module (biaxial) creates parallax

effect. In addition, since it has a rather small FOV, the light reflected from the target at very close distances cannot be collected by the receiver lens because it reflects with a very wide angle with respect to receiver optical axis.

On the other hand, as the distance increases, the amount of power incident on the detector falls inversely proportional to the distance from the target.

The simulation was performed assuming the visibility distance is 0.5 km for fog. Attenuation constant is estimated to be 6.20 for foggy air. Atmospheric transmission varies depending on the distance.

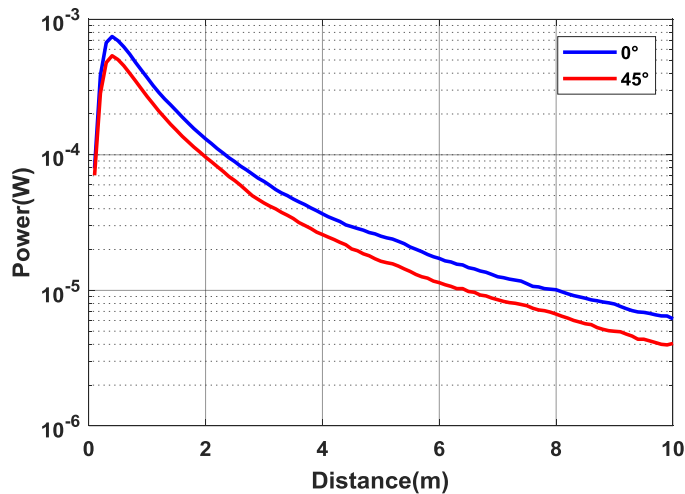


Figure 2.11 Power with respect to distance in foggy air

To evaluate whether the amount of power incident on the detector conforms to the LPS requirements, SNR analysis was carried out using the specifications of the detector and the preamplifier circuit.

The lowest amount of power incident on the detector was obtained at 45° in foggy weather conditions. Thus,  $minimum\ current = 4\mu W \times 0.6 \frac{A}{W} = 2.4\ \mu A$

SNR is mainly affected by solar background radiation. Solar radiation causes a steady current in the receiver which in turn generates shot noise. Therefore, shot

noise is included in TIA which also reduces SNR. Even though solar radiation on the ground changes with respect to time of the day and year, total solar radiation is about  $100\text{mW}/\text{cm}^2$  at ground under clear weather conditions [2].

Background radiation is calculated using the following equation [2].

$$P_B = \frac{I\theta_t^2\rho\pi r^2 F}{4} \quad (36)$$

where  $I$ ,  $\rho$  and  $F$  are total solar radiation on the ground surface, ground reflection coefficient and ratio of background power contained in the optical bandpass filter to the total solar radiation, respectively.  $F$  is expressed with the following equation [2].

$$F = \frac{\frac{15}{\pi^4} \left(\frac{h\nu}{kT}\right)^4}{\frac{h\nu}{e^{kT}} - 1} d\lambda/\lambda \quad (37)$$

where  $\frac{h\nu}{kt}$  is the ratio of photon energy at laser wavelength to the thermal energy at solar temperature of  $T = 6000\text{K}$  and  $\frac{d\lambda}{\lambda}$  is the fractional bandwidth of the optical filter.

Using the parameters of the developed LPS for solar radiation of  $100\text{ mW}/\text{cm}^2$ , background power due to solar radiation is approximately  $30\mu\text{W}$  for a ground reflection coefficient of 1. The shot noise root mean square (RMS) current per square root Hz ( $i_b$ ) is given by the following equation [2].

$$i_b = \sqrt{2q_e P_B S} \quad (38)$$

where  $S$  is responsivity of the detector. The shot current in a bandwidth of  $49\text{ MHz}$  is then approximately  $19\text{ nA}$ .

Total RMS noise current ( $i_n$ ) for the PIN photodetector and TIA combination can be calculated using the following equation [2].

$$i_n^2 = i_b^2 + i_{na}^2 B \quad (39)$$

where  $i_{na}$  is input-referred current noise of TIA. Using the input-referred current noise parameter of the TIA for the developed LPS at 60k gain, total rms current noise is 20 nA.

The minimum SNR is then equal to  $20\log\left(\frac{2.4\mu A}{20nA}\right) = 42dB$ . SNR values with respect to target distance are given in Figure 2.12.

Probability of detection with respect to SNR assuming a FAR of  $\frac{10^{-4}}{s}$  is calculated using the following equation [20].

$$P_D = \frac{1}{2} + \frac{1}{2} \operatorname{erf}\left(\frac{SNR - TNR}{\sqrt{2}}\right) \quad (40)$$

where  $P_D$ ,  $\operatorname{erf}$  and  $TNR$  are probability of detection, error function and threshold to noise ratio, respectively.

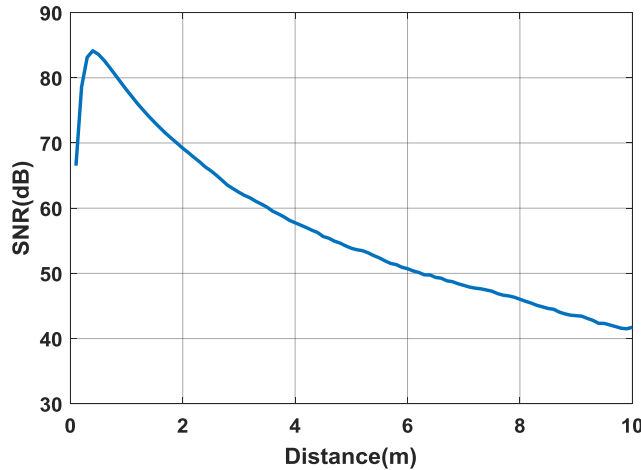


Figure 2.12 SNR with respect to target distance

Threshold to noise ratio is given by [20]:

$$TNR = \sqrt{-2\ln(2\sqrt{3} \cdot \tau \cdot FAR)} \quad (41)$$

where  $\tau$  is laser pulse width. Threshold to noise ratio at 100 ns pulse width is:

$$TNR = \sqrt{-2 \ln \left( 2\sqrt{3} \cdot 100ns \cdot \frac{10^{-4}}{s} \right)} = 6.6005; \quad (42)$$

The minimum SNR value required for 100% probability of detection is 10.5 dB. In the analysis made according to our LPS hardware design parameters, the calculated SNR values for FAR of  $\frac{10^{-4}}{s}$  at distances between 0.5 m - 10 m showed 100% probability of detection. This result proves that using the same transmitter lens in the receiver module reveals sufficient optical performance.

## 2.4 Temperature Dependence of Laser Diode Central Wavelength

The LPS uses InGaAs/GaAs strained quantum well laser which emits at 905nm. Due to nature of semiconductor laser diodes, the central wavelength depends on direct band gap energy of the semiconductor material as well as the concentration of dopants and the configuration of the active layer [13]. In order to examine the central wavelength shift due to temperature change, peak emission wavelength of the laser diode was measured using optical spectrum analyser at 0-70°C.

Test was performed by increasing the laser diode temperature by hot plate and the temperature data was taken from laser diode leads using thermocouple. Error margin of thermocouple was assumed to be  $\pm 5$  °C. On the other hand, error margin of the central wavelength measurement was assumed to be  $\pm 1$  nm. After applying a linear

fit to data points based on temperature measurement error margin, temperature coefficient wavelength was calculated to be 0.32 nm/K with standard error of 0.047. The data sheet of the laser diode specifies temperature coefficient wavelength as 0.28 nm/K.

Figure 2.13 shows that central wavelength increases with temperature. This behaviour can be explained as the decrease in band gap energy as well as the increase in quantum well period.

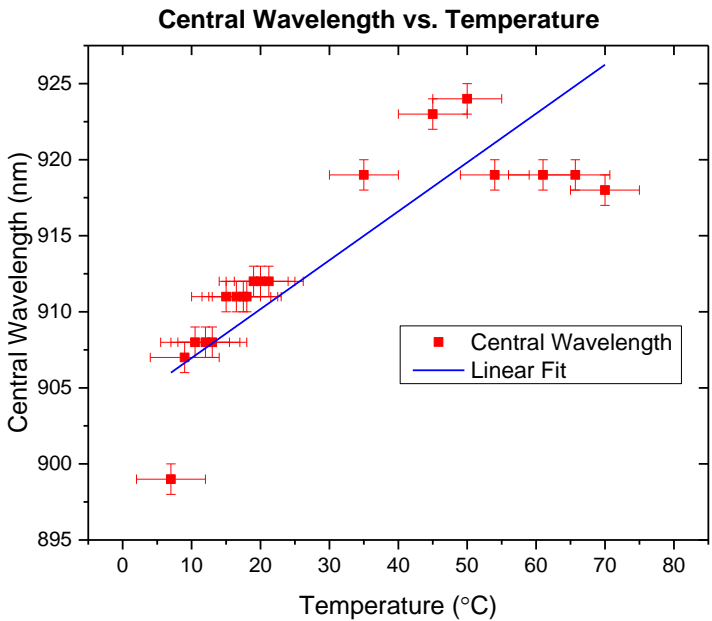


Figure 2.13 Central wavelength shift due to temperature increase

Laser emission spectrum at three different temperatures is shown in Figure 2.14. It is obvious that intensity of the peak emission wavelength decreases with temperature even at the same current level. This is a result of threshold current to increase with temperature in order for the stimulated emission to occur. Since stimulated emission also depends on carrier concentration on active layer, the probability for emitting recombination processes decreases as the temperature rises [13].

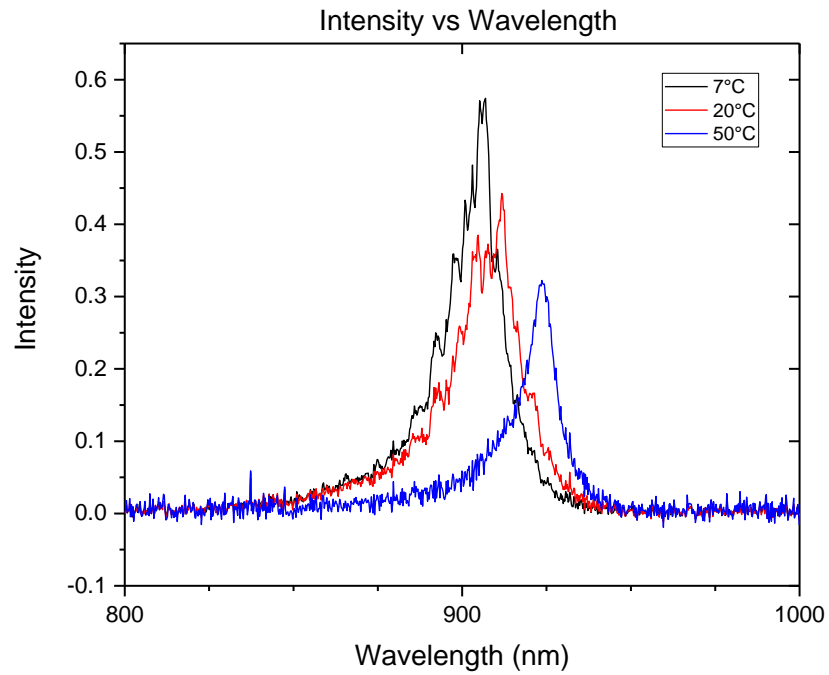


Figure 2.14 Laser emission spectrum at three different temperatures

## 2.5 Interference Bandpass Filter Design

In order to increase optical performance of the LPS, an optical bandpass filter was designed to block the background light having a wavelength ranging outside of the laser's emission spectrum at its all operation temperatures. Interference filter was designed using Open Filters software which is freely available [21]. Thicknesses for a Distributed Brag Reflector (DBR) based filter was provided as initial condition and needle optimization method was used to obtain desired transmission rate for wavelengths between 860 nm and 940 nm while blocking the background light. Filter substrate is BK7 with a thickness of 2 mm. Layer structure is given in Table 2.3.

Table 2.3 Optical bandpass filter layer structure

Layer #	Material	Thickness(nm)	Layer #	Material	Thickness(nm)
1	TiO <sub>2</sub>	167.661	22	SiO <sub>2</sub>	103.652
2	SiO <sub>2</sub>	21.945	23	TiO <sub>2</sub>	115.360
3	TiO <sub>2</sub>	58.818	24	SiO <sub>2</sub>	256.741
4	SiO <sub>2</sub>	374.017	25	TiO <sub>2</sub>	69.006
5	TiO <sub>2</sub>	259.755	26	SiO <sub>2</sub>	136.917
6	SiO <sub>2</sub>	93.113	27	TiO <sub>2</sub>	86.557
7	TiO <sub>2</sub>	75.274	28	SiO <sub>2</sub>	333.474
8	TiO <sub>2</sub>	194.201	29	TiO <sub>2</sub>	57.498
9	TiO <sub>2</sub>	143.439	30	SiO <sub>2</sub>	241.769
10	SiO <sub>2</sub>	78.778	31	TiO <sub>2</sub>	100.240
11	TiO <sub>2</sub>	164.330	32	SiO <sub>2</sub>	100.265
12	SiO <sub>2</sub>	75.622	33	TiO <sub>2</sub>	94.133
13	TiO <sub>2</sub>	147.702	34	SiO <sub>2</sub>	79.759
14	SiO <sub>2</sub>	303.932	35	TiO <sub>2</sub>	42.830
15	TiO <sub>2</sub>	70.896	36	SiO <sub>2</sub>	83.921
16	SiO <sub>2</sub>	111.328	37	TiO <sub>2</sub>	217.032
17	TiO <sub>2</sub>	125.774	38	SiO <sub>2</sub>	22.148
18	SiO <sub>2</sub>	118.836	39	TiO <sub>2</sub>	215.150
19	TiO <sub>2</sub>	83.575	40	SiO <sub>2</sub>	82.467
20	SiO <sub>2</sub>	377.253	41	TiO <sub>2</sub>	45.249
21	TiO <sub>2</sub>	59.773			

Transmission curve of the filter is given in Figure 2.15. Filter has a transmission curve above 90% for wavelengths between 860 nm - 940 nm at 0 degree incidence angle. This range also covers the central wavelength shift due to temperature change while blocking the visible spectrum.

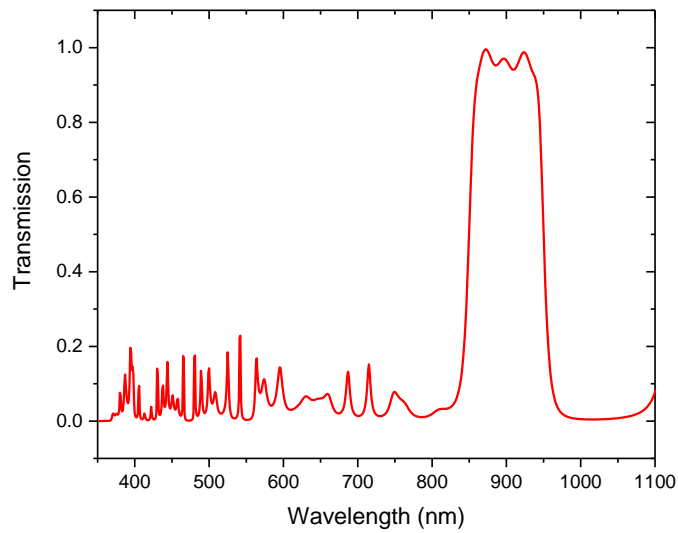


Figure 2.15 Transmission spectrum of the bandpass filter

## 2.6 Review

In order to meet the LPS technical requirements, a special optical design has been performed with the help of Zemax software for the transmitter and receiver module. During the design, an attempt was made to produce an optimum solution by considering the cost and performance balance. Performance analysis was also performed using the same lens for both transmitter and receiver module. Results of Monte Carlo analysis in foggy weather conditions were evaluated with the developed LPS hardware design parameters. In addition, SNR and probability of detection calculations based on various target distances have been presented. Temperature dependence of central wavelength has been measured which in result affects the optical band pass filter design. According to central wavelength shift due to temperature change, an optical bandpass filter was designed to block the background light having a wavelength ranging outside of the laser's emission spectrum.



## **CHAPTER 3**

### **MATHEMATICAL MODEL**

System modelling of Direct Detection Short Pulsed LPS was performed in Matlab Simulink environment using the mathematical model described in detail in Chapter 1 [22]. The transmitter, receiver and signal processing modules of the LPS were simulated using parameters reflecting the exemplary hardware design. The LPS Simulink Model is given in Appendix C.

The model identifies the presence and distance to the target by transmitting the laser signal, interacting with the target through propagation in atmosphere, collecting the reflected laser on the detector and processing the relevant signals by various signal processing algorithms.

#### **3.1 Transmitter Module**

Transmitter module was modelled based on the mathematical principles described in Chapter 1. Thus, laser pulse is modelled in Gaussian form. Modelling has been performed using laser pulse width of 10 ns (FWHM) and the peak power of 50W. The pulse repetition frequency is 10 kHz. Figure 3.1 shows the Simulink model of the transmitter module and Figure 3.2 displays the generated outputs.

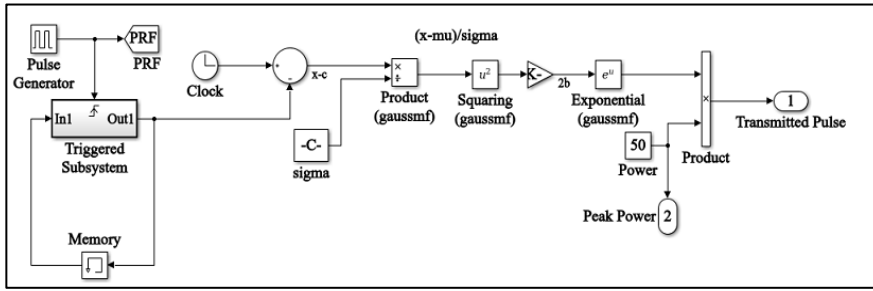


Figure 3.1 Simulink model layout of transmitter block

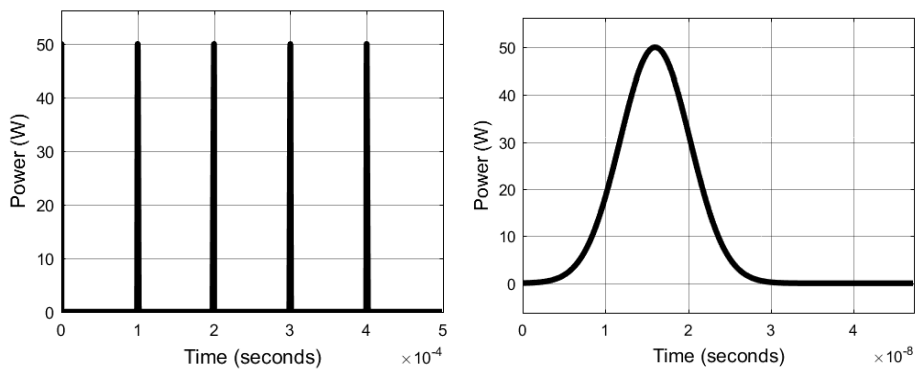


Figure 3.2 (a) Pulse repetition frequency (b) Gaussian pulse output

### 3.2 Receiver Module

The laser pulse transmitted by the transmitter module arrives the detector by propagating in the atmosphere twice the distance to the target. Since the laser pulse travels at the speed of light, the delay time is expressed by Equation (5).

During propagation in the atmosphere, the laser pulse is attenuated by scattering through the atmosphere, surface reflection, target surface interaction area, distance and the optical transmission of the receiver. In addition, thermal noise, photon counting noise, background noise are added to the attenuated signal.

The modelling was carried out using a laser projection with a divergence angle of 40 degrees. The laser solid angle can be calculated by the following equation.



### 3.2.1 Signal to Noise Ratio

The echo signals reflected from the target are converted to current output by the PIN detector located on the receiver module. The current is then converted into voltage by amplifying the signal with the aid of the TIA circuit. The voltage signal is then amplified at a constant gain to be processed by the signal processing module. Noise modelling was done using the PIN detector and preamplifier circuit parameters. The SNR is defined as the ratio of the signal to the current noise of the detector. The SNR on the PIN detector is expressed by the following equation [23].

$$SNR_{PIN} = \frac{P_{signal}}{P_{thermal} + P_{amp} + P_{dark} + P_{shot} + P_{back}} \quad (46)$$

The power incident on the detector due to reflected laser pulse is expressed by the following equation [23].

$$P_{signal} = (P_R S)^2 R_{load} \quad (47)$$

The detector load resistor, which converts the detector output current into voltage, is shown in Figure 3.4.

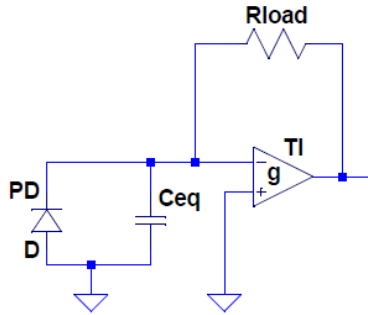


Figure 3.4 Representative schematic view of TIA

Detector sensitivity is represented by  $S$  [A/W]. Thermal noise is given by the following equation [23].

$$P_{thermal} = 4kTB \quad (48)$$

$k$  represents Boltzmann constant,  $T$  is temperature and  $B$  is detector bandwidth.

Noise due to amplifier circuit is given by the following equation [23].

$$P_{amp} = (I_{amp}^2 + \frac{V_n^2}{R_{load}^2})BR_{load} \quad (49)$$

Quantum shot noise depending on received laser signal is given by the following equation [23].

$$P_{shot} = 2eP_R SBR_{load} \quad (50)$$

Dark current is the current generated by the detector itself when there is no light incident on the PIN detector [23].

$$P_{dark} = 2eI_{dark} SBR_{load} \quad (51)$$

Background noise is due to the sun light reflected from the target.

$$P_{back} = 2eP_b SBR_{load} \quad (52)$$

The background solar radiation  $P_b$  is expressed by the following equation [23].

$$P_B = \frac{I\beta^2\rho\pi D^2 F}{16} \quad (53)$$

where  $I$ ,  $\beta$  and  $F$  are total solar radiation, receiver FOV and the ratio of background noise within the filter bandwidth to the solar radiation, respectively.

Values used in the Simulink model are as the following.

$$B = 100 \text{ MHz}; I_{dark} = 10 \text{ nA}; \rho = 0.4; P_T = 50 \text{ W}; D = 20 \text{ mm}; T_{op} = 0.6;$$

$$\lambda = 905 \text{ nm}; R_v = 900 \text{ m}; P_B = 5.19 \times 10^{-17} \text{ W}; k = \frac{1.38 \times 10^{-23} \text{ J}}{K};$$

$$T = 300 \text{ K}; I_{amp} = \frac{1.3 \times 10^{-15} \text{ F}}{\sqrt{\text{Hz}}}; V_n = \frac{7 \times 10^{-9} \text{ V}}{\sqrt{\text{Hz}}}; S = \frac{0.6 \text{ A}}{\text{W}};$$

$$e = 1.6 \times 10^{-19} \text{ C}; R_{load} = 10 \text{ k}\Omega$$

Figure 3.5 shows the noise modelling using the equations above.

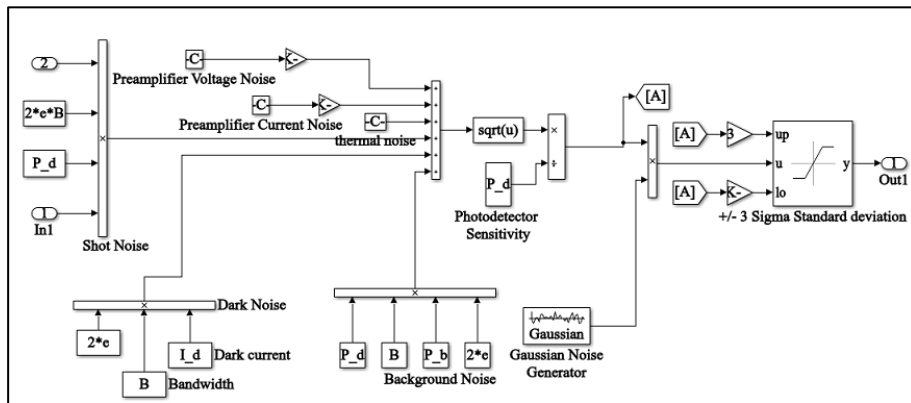


Figure 3.5 Noise modelling layout

Therefore, the laser pulse waveform transmitted to the target and the reflected echo signal waveform from the flat target of 0.5 m x 0.5 m at 10 m are shown in Figure 3.6.

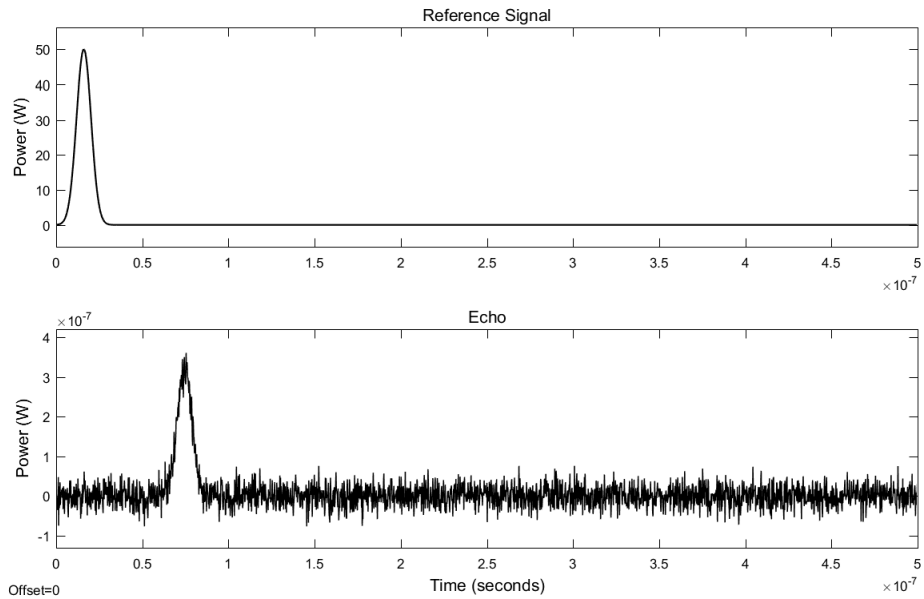


Figure 3.6 Simulink model output for reference laser signal as well as reflected echo signal with the addition of noise

Detector and preamplifier circuit modelling is given in Figure 3.7.

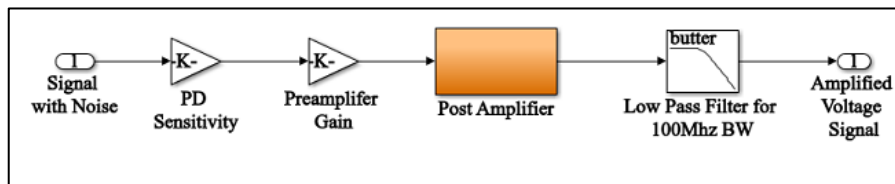


Figure 3.7 Detector and preamplifier circuit modelling layout

The SNR value required to meet the detection probability of at least 95% and the FAR of at least  $10^{-4}$ /s was calculated to be at least 10 dB. The minimum SNR value in the Simulink model is assumed to be 10 dB, and all signals below this value are considered noise.

### 3.3 Signal Processing Module

#### 3.3.1 Echo Signal Sampling

The echo signal is converted to voltage by the receiver module and carried to the signal processing module. In order to be processed by the signal processing module, the analog signal must first be digitally converted by means of an ADC. The modelling was performed at a sampling rate of two channels, 14 bits, 250 MHz. In this method, the echo signal is sampled by two parallel 250 MHz clocks with some phase difference. Thus, the sampling rate doubles. Two counters in parallel at equal speed with some phase difference are created by the on-chip phased-locked-loop (PLL) on the external 250 MHz counter Field Programmable Gate Array (FPGA). The dual channel ADC output and the counter information are stored in two separate memories. In addition, since the dual channel ADC outputs one channel at a time, samples are combined using the controller. With this method, the signal can be sampled at 500 MHz using 250 MHz ADC. This method is shown in Figure 3.8.

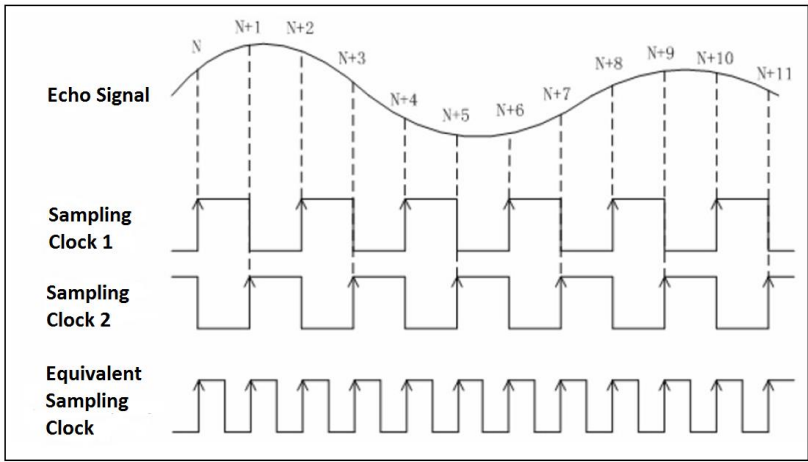


Figure 3.8 Two channel ADC operating principle [22]

The ADC module and ADC output of the LPS Simulink model are shown in Figure 3.9 and Figure 3.10, respectively.

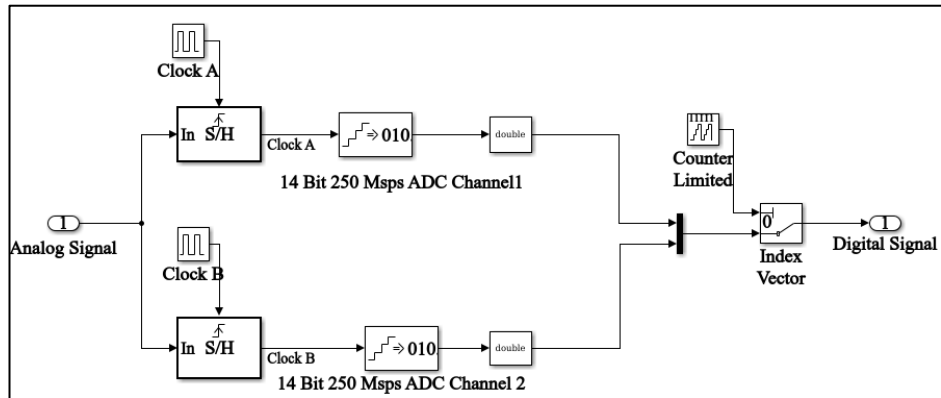


Figure 3.9 ADC Model

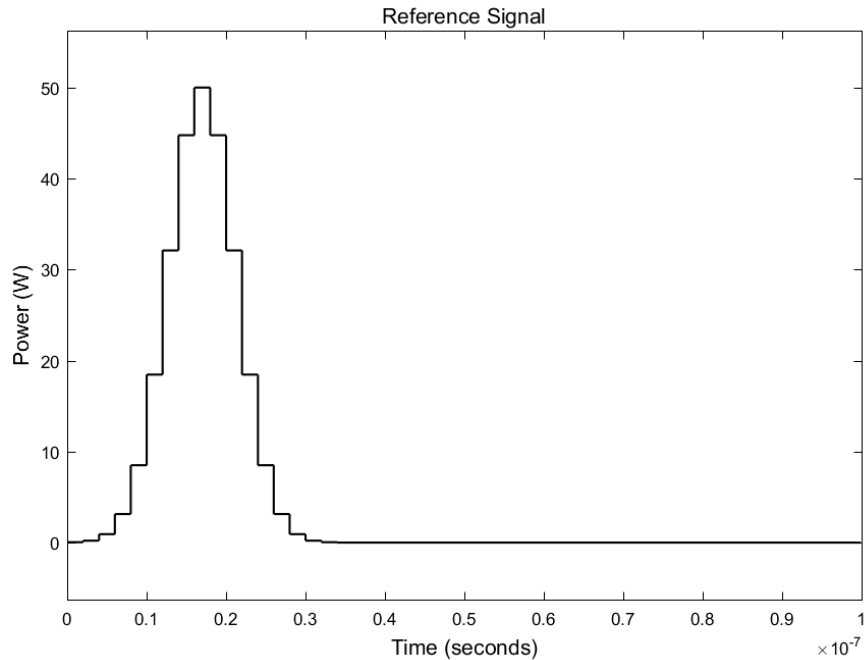


Figure 3.10 ADC model output

### 3.3.2 Equivalent In-phase Echo Signal Averaging

The echo signal is attenuated depending on distance, target type, environmental conditions, and so on. This attenuation causes the echo signal to be lost in the noise. Thus, the target signal that is below the threshold SNR value is perceived as noise. In the modelling, a multiple in-phase echo signal averaging method was applied to

increase SNR. In this method, echo signals reflected from the target are sampled in the ADC and collected in the memory. The signal samples are then averaged according to their position in time space. This method is expressed mathematically below.

Echo signal can be represented based on time as the following equation [20].

$$x(t) = A \cdot s(t) + w(t) \quad (54)$$

where  $s(t)$ ,  $A$  and  $w(t)$  are normalized pulse, echo signal amplitude and noise, respectively.

$N$  number of echo signals are sampled. In each echo signal, the number of sampling points  $M$  and the sampling interval  $\Delta t$ , the value of the sampling point ( $j = 0, 1, \dots, N-1$ ) in the echo signal is calculated using the following equation [20].

$$x(t_i + j\Delta t) = A \cdot s(t_i + j\Delta t) + w(t_i + j\Delta t) \quad (55)$$

$t_i$  is the sampling start time of the  $i^{\text{th}}$  echo signal and the sampling start time of the other echo signals must be related to each other. The following notation can be used to simplify Equation (55).

$$x_{ij} = A \cdot s_{ij} + w_{ij} \quad (56)$$

$M$  number of sampling values of an echo pulse is recorded and the next pulse signal samples are accumulated with respect to the position in the time space with the number of sampling values of the previous pulses. By sampling and collecting  $N$  number of echo pulses, in-phase average of any  $j$  points in the echo pulse is given by the following equation [20].

$$\frac{1}{N} \sum_{i=0}^{N-1} x_{ij} = \frac{A}{N} \sum_{i=0}^{N-1} s_{ij} + \frac{1}{N} \sum_{i=0}^{N-1} w_{ij} \quad (57)$$

This equation can be rearranged as follows.

$$\frac{1}{N} \sum_{i=0}^{N-1} x_{ij} = A \cdot s_j + \frac{1}{\sqrt{(N)}} \sigma \quad (58)$$

where  $\sigma$  is equal to  $\sqrt{w_{ij}}$ .

The LPS Simulink block layout of in-phase echo signal averaging is shown in Figure 3.11.

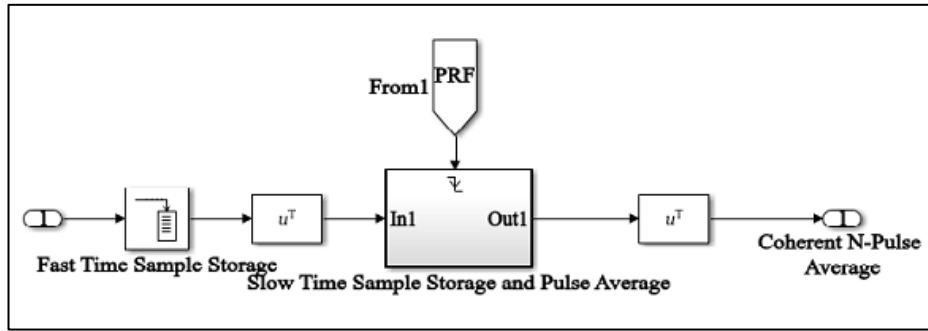


Figure 3.11 Averaging module layout

The average for a different number of echo signals at 5 m distance is shown in Figure 3.12. Therefore, as the N value increases, the noise decreases and the SNR value increases. This is explained by the random nature of the noise that exists in the signal. The SNR gain is shown in the following expression [20].

$$SNR_i = \frac{A^2}{\sigma^2}; \quad SNR_0 = N \cdot SNR_i \quad (59)$$

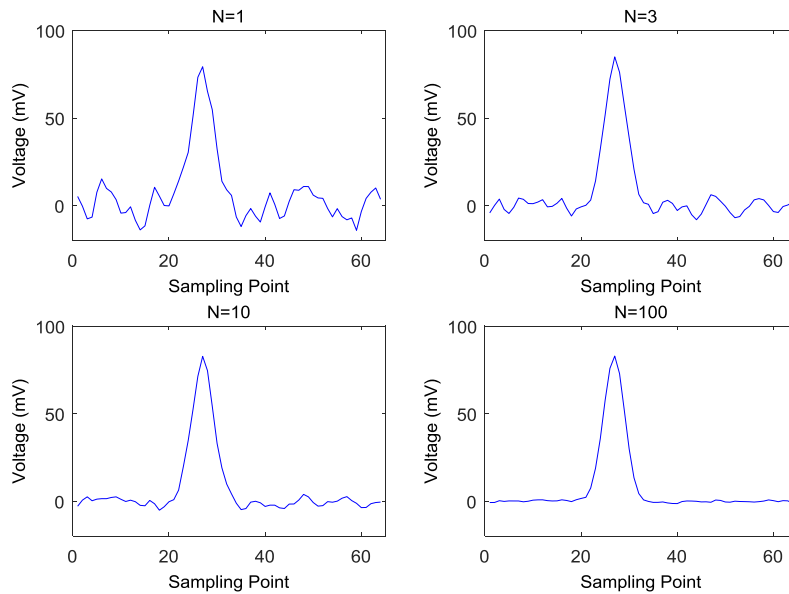


Figure 3.12 In-phase echo signal averaging for N=1, 3, 10 and 100

Therefore, the SNR is increased proportional to the number of echo signals collected. However, this method has a disadvantage. As the number of collected echo signals increases, the response time of the LPS increases. This increases the miss probability at high speed without the target being detected. The solution is to increase the pulse repetition frequency. If the pulse repetition frequency is increased, the required number of echo signals from the target will be collected in less duration. In Simulink model, the pulse repetition period is  $100\mu\text{s}$ . According to this time, the LPS model has a response time of maximum 1 ms.

### 3.3.3 Range Calculation

In LPS Simulink model, the distance to the target was calculated by time of flight method. The accuracy of distance measurement according to this method depends on the accuracy of the time of flight calculation. In literature there are various methods

to measure time of flight duration, some of which are leading edge discriminator, peak estimator and cross correlation. In Chapter 1, all of these methods are described and compared in detail. Due to performance advantages of cross correlation method the LPS Simulink model was created using the cross-correlation method.

The mathematical model of the echo signal is expressed as follows [20].

$$x[n] = A \cdot s[n - n_0] + w[n], \quad 0 \leq n \leq M - 1 \quad (60)$$

where  $n_0$  and  $M$  are the sampling point during the delay of the echo signal and the sampling length, respectively.

The cross correlation method calculates the  $p(k)$  peak position of the cross correlation function as  $n_0$  [20].

$$n_0 = \arg \max p(k); \quad p(k) = \sum_{n=0}^{M-1} x[n]s[n - k] \quad (61)$$

Range is calculated using the following equation.

$$R = \frac{1}{2} \cdot c \cdot \Delta t = \frac{1}{2} \cdot c \cdot n_0 \cdot \Delta \quad (62)$$

where  $\Delta$  and  $\Delta t$  are the sampling interval in equality and the time of flight for the calculated pulse, respectively.

Equation (62) implies that the accuracy of the distance measurement is directly proportional to the sampling rate of the ADC. The distance is measured with accuracy of 2 ns at the speed of 500 MHz obtained by ADC method used in the modelling. This corresponds to a distance of 30 cm. A high-speed ADC can be used to increase the resolution. However, using a high speed ADC makes the electronics circuit complicated. It also increases the cost significantly. Thus, a different method is applied in the model called delayed cross-correlation method.

### 3.3.3.1 Delayed Cross Correlation

In order to calculate the time of flight by the cross correlation method, it is necessary to calculate the cross-correlation peak position. If the time of flight is an integer multiple of the sampling interval, the cross correlation peak is sampled. Otherwise the point next to the peak point is sampled. This causes a faulty time of flight measurement. If the cross correlation resolution is not enough to sample the peak point, the problem resulting from the sampling rate can be mitigated by modifying the time of flight equation. Thus, the delayed cross-correlation equation is expressed as the following [20].

$$\begin{aligned} p(k+d) &= \sum_{n=0}^{M-1} x[n]s[n-(k+d)] \\ &= \sum_{n=0}^{M-1} x[n]s[(n-d)-k] \end{aligned} \quad (63)$$

where  $d$  is the delay time. In addition, this time must be smaller than the sampling interval. As can be understood from the above equation, in order to calculate the delayed cross-correlation function, it is necessary to calculate the cross-correlation by applying a delay to the reference signal as  $d$ . The delayed cross-correlation expression can be simplified with the following changes made in the notation [20].

Therefore,  $s_d[n] = s[n-d]$  and  $p_d(k) = p(k+d)$

Then,

$$p_d(k) = \sum_{n=0}^{M-1} x[n]s_d[n-k] \quad (64)$$

When  $d = 0, \frac{1}{K}\Delta, \frac{2}{K}\Delta, \dots, \frac{K-1}{K}\Delta$ , the delayed reference signals  $s_d^0[n], s_d^1[n], s_d^2[n], \dots, s_d^{K-1}[n]$  are shown in Figure 3.13.

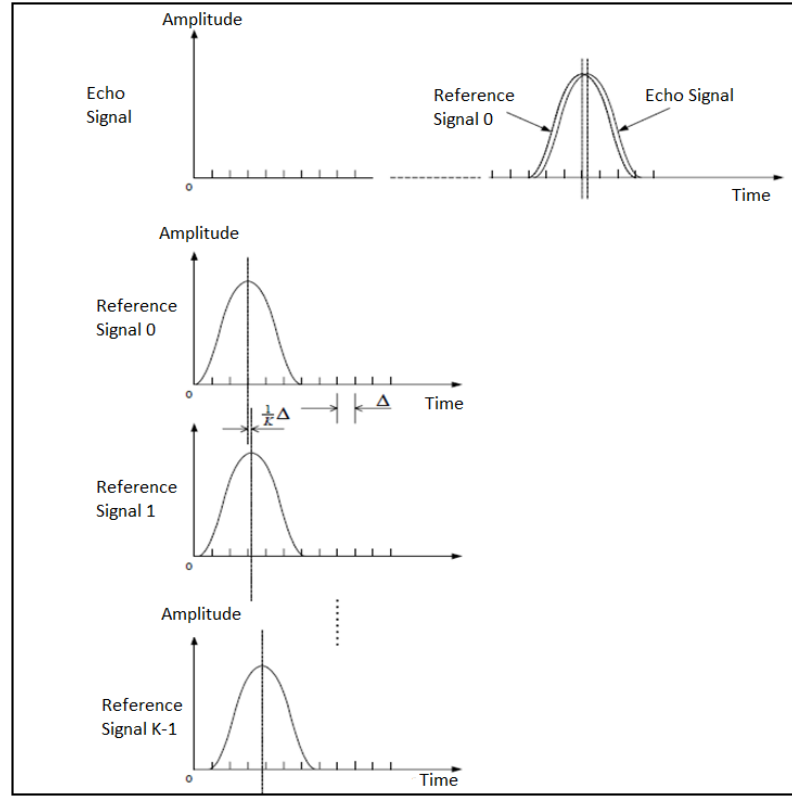


Figure 3.13 A schematic of delayed cross correlation method [20]

Delayed cross correlation functions can be expressed as the following [20].

$$\begin{aligned}
 p_d^0(k) &= \sum_{n=0}^{M-1} x[n]s_d^0[n-k] \\
 p_d^1(k) &= \sum_{n=0}^{M-1} x[n]s_d^1[n-k] \\
 &\vdots \\
 p_d^{K-1}(k) &= \sum_{n=0}^{M-1} x[n]s_d^{K-1}[n-k]
 \end{aligned} \tag{65}$$

If the maximum of the delayed cross-correlation is  $p_d^a(k)$  ( $0 < a < K - 1$ ), time of flight can be calculated by the following equation [20].

$$\Delta t = n_0 \cdot \Delta + a \cdot \frac{1}{K} \Delta \quad (66)$$

Thus, the distance measurement accuracy is increased by K times. In Simulink model, cross correlation calculation was performed with 5 different delayed reference signals. Therefore, the distance measurement accuracy was improved by 5 times. Since a 500 MHz ADC was used in the model, the distance measurement accuracy is 30 cm. However, the accuracy of the distance measurement after applying the delayed cross-correlation method is 7.5 cm.

The LPS Simulink Model delayed cross-correlation block is shown in Figure 3.14.

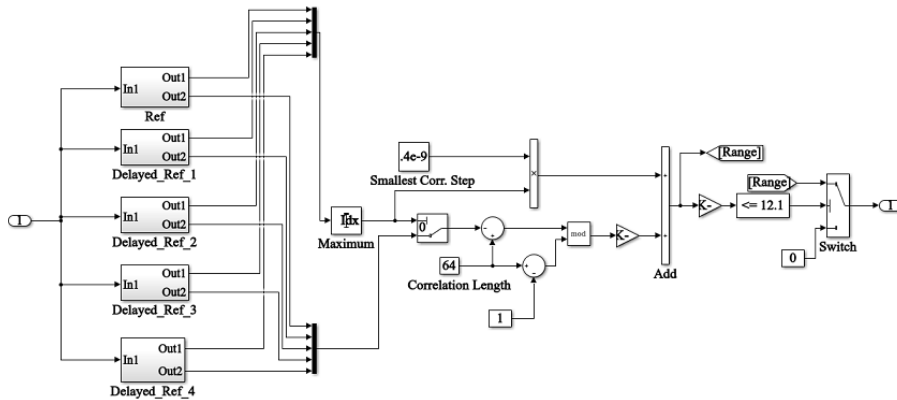


Figure 3.14 Delayed cross correlation block layout

The following table shows the mathematical model distance outputs by using 0.5 m x 0.5 m and 1 m x 1 m fixed square plate targets for different distances. As can be seen from the results, all the distance outputs are within the theoretical calculated 7.5 cm accuracy. The sensor model does not provide a detection signal for targets farther than 12 m to reduce the possibility of false alarms.

Table 3.1 LPS Simulink model target range output

<b>True Range (m)</b>	<b>Range Output (m) for Small Target (0.5 m x 0.5 m)</b>	<b>Range Output (m) for Large Target (1 m x 1 m)</b>
0.57	0.62	0.62
1.13	1.1	1.1
2.56	2.6	2.6
4.75	4.82	4.82
6.19	6.2	6.2
8.42	8.42	8.42
9.34	9.38	9.38
10.3	10.34	10.34
11.76	11.78	11.78

### 3.4 Review

In the Simulink environment, a modelling study was carried out in which all submodules were simulated by example hardware design parameters and the performance of the some signal processing algorithms was evaluated. Simulink model enables a high detailed design of all submodules with minimal effort before design validation and prototyping activities. It also facilitates design by providing a rapid optimization of all design parameters of the device characteristic by iteration method.



## CHAPTER 4

### CONCLUSIONS

With the evolving laser technology, LIDARs found many applications such as obstacle detection, road environment detection, atmospheric remote sensing and meteorology, speed measurements and proximity detection. In particular, semiconductor laser and photodetector technology made LIDARs more compact and affordable. However, there is still space for improvement in particularly from system design point of view. Designing an LPS necessities multi-disciplinary approach including optical design, analog and digital circuit design and software/firmware development. Within the scope of this thesis, transmitter and receiver optical design, mathematical modelling and circuit design studies have been performed.

Laser diode was modelled based on astigmatic characteristic and aperture size using Zemax. Divergence angles of  $\theta_x = 0.185^\circ$ ,  $\theta_y = 0.013^\circ$  were achieved thanks to custom designed single aspherical lens. Lens design was realized based on low cost and easy to manufacture specifications. Optical performance analysis showed that the developed LPS can detect targets at distances between 0.5 m and 10 m at a false alarm rate of  $\frac{10^{-4}}{s}$  with 100% for probability at foggy air. Central wavelength of the laser diode was measured at temperatures between 0 and 70 °C using a spectrometer. An optical bandpass filter consisting of 20 layers TiO<sub>2</sub>/SiO<sub>2</sub> stacks was designed to pass over 90% between 860 nm and 940 nm. In addition, bandpass filter blocks the background light having a wavelength ranging outside of the laser's emission spectrum at its all operation temperatures.

A laser diode driver which generates 10 A current pulses of 100 ns width at 10 kHz pulse repetition frequency was designed and verified with spice simulations. The

developed LPS is expected to measure distances with less than 2.7 cm resolution thanks to the Time-to-Digital Converter (TDC) circuit. A distance measurement rate of 10000 per second is expected with our LPS design.

## APPENDIX A

### LPS ELECTRONICS

#### Laser Diode Driver Circuit

Transmitter module of the LPS is essentially a pulsed laser diode driver circuit which generates high current pulses at the pulse repetition frequency determined by the processor module. Transmitter circuit also generates a 'start flag' after a certain delay from laser emission. This signal is then acquired by the processor module in order to start the digital counter.

A Near Infrared (NIR) single emitter pulsed laser diode has been used as laser source in transmitter module. The efficiency of such single emitter laser diodes is usually 1 W/A [24]. The laser diode driver circuit generates 10 A current pulse at 100ns pulse width which is roughly equivalent to 10 W optical peak power emission by the laser. Since the laser diode used has a maximum duty cycle of 0.1%, maximum pulse repetition frequency is limited to 10 kHz.

Producing such high current pulses at such short durations requires special attention to schematic as well as PCB design. It was decided to use high power Metal-Oxide Semiconductor Field-Effect Transistor (MOSFET) instead of avalanche transistor since the latter requires very high voltage for operating at the avalanche regime. However, switching on and off power MOSFETs at 100 ns duration is not possible using microcontroller I/Os due to high current demand of MOSFET gate. This is a result of gate capacitance of MOSFETs. Thus, it is inevitable to use MOSFET gate driver circuit which can be triggered by CMOS or TTL compatible logic. Generation of start flag may be realized using a comparator circuit which detects current pulse

generation and produces low or high enable signal. Block diagram of laser driver circuit is shown in Figure A.1.

Spice simulations were performed providing 10 kHz CMOS input signal to verify current pulse and start flag signals. Simulation outputs are shown in Figure A.2. Current peak is at around 10A and the pulse has a width of around 100ns. The delay between current pulse and start flag is around 40ns.

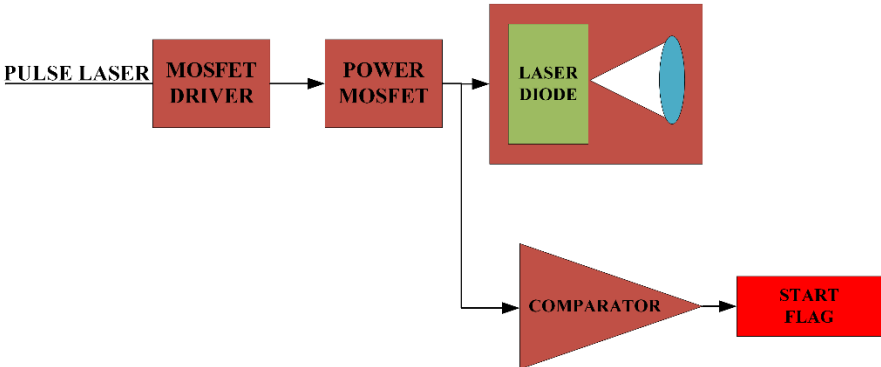


Figure A.1 Laser diode driver block diagram

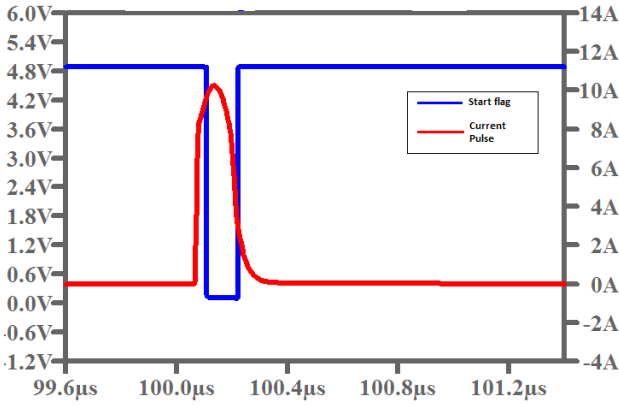


Figure A.2 Spice simulation of current pulse and start flag

## Transmitter PCB Layout

We decided to use 4 layer stack up to minimize electromagnetic interference due to switching current pulses. During PCB layout, power and ground tracks were drawn to be wide enough in order to carry high current. Reserving ground and power planes during layout enables less parasitic inductance. Bypass capacitors were placed very close to each integrated circuit. Short tracks were drawn for providing current with laser diode so that parasitic inductance is decreased. Any extra parasitic inductance increases the laser pulse rise time causing faulty measurements. In order to prevent high speed signal reflections, 50 ohm controlled impedance tracks were drawn for start flag signal. Latest 3D view of transmitter PCB is shown in Figure A.3.



Figure A.3 3D view of transmitter PCB

Each layer view is shown in Figure A.4.

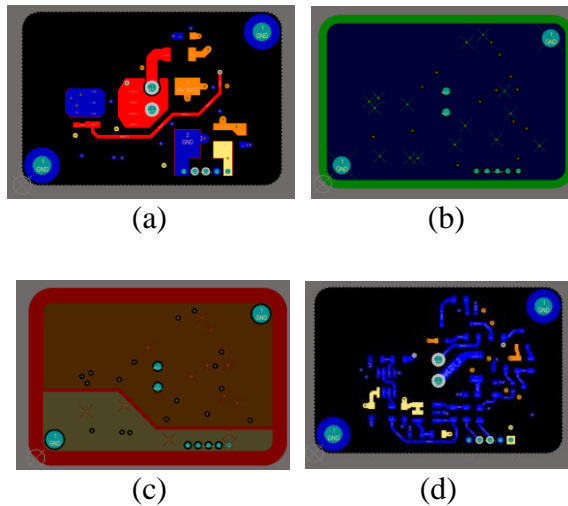
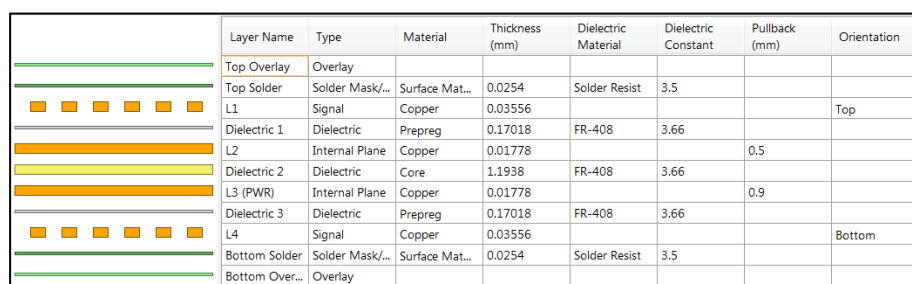


Figure A.4 (a) Signal (Top) layer (b) Ground layer (c) Power layer  
(d) Signal (Bottom) layer

Layer stack-up is also shown in Figure A.5.



Layer Name	Type	Material	Thickness (mm)	Dielectric Material	Dielectric Constant	Pullback (mm)	Orientation
Top Overlay	Overlay						
Top Solder	Solder Mask/...	Surface Mat...	0.0254	Solder Resist	3.5		
L1	Signal	Copper	0.03556				Top
Dielectric 1	Dielectric	Prepreg	0.17018	FR-408	3.66		
L2	Internal Plane	Copper	0.01778			0.5	
Dielectric 2	Dielectric	Core	1.1938	FR-408	3.66		
L3 (PWR)	Internal Plane	Copper	0.01778			0.9	
Dielectric 3	Dielectric	Prepreg	0.17018	FR-408	3.66		
L4	Signal	Copper	0.03556				Bottom
Bottom Solder	Solder Mask/...	Surface Mat...	0.0254	Solder Resist	3.5		
Bottom Over...	Overlay						

Figure A.5 Transmitter layer stack-up

## Receiver Circuit

Duty of receiver circuit is to detect the reflected laser signal and amplify it to readable electronic signal levels by microcontroller. The challenge is to detect very high speed and attenuated laser signal and amplify it without losing any signal. This requires use of high speed detector and TIA. In addition, echo signal is not digitized by an ADC. Instead, analog signal peak point is sampled using a high pass filter as explained in section 1.7.2. Sampled point is detected by a comparator which then generates 'stop flag'.

The problem with the analog peak estimator is the linearity of TIA is distorted when the signal is outside the dynamic range of TIA. Thus, it is important to choose a TIA which has a wide dynamic range. Otherwise, a faulty sampling of the peak will cause false measurements. MAX3806 TIA from Maxim Integrated has been selected to use in the circuit design of receiver. It has a 130dB dynamic range which enables to amplify signal inputs from  $42\text{nA}_P$  ( $\text{SNR} = 3$ ) to  $40\mu\text{A}_P$  [25]. This capability also eliminates the use of variable auto gain amplifier depending on the signal amplitudes.

Block diagram of the receiver circuit is given in Figure A.6.

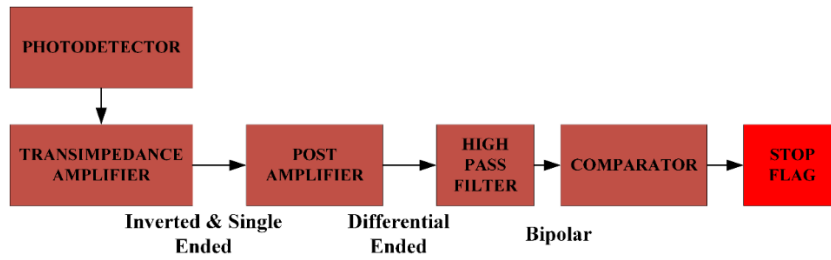


Figure A.6 Receiver block diagram

Current output of the PIN photodetector is amplified by 60000 or 30000 times depending on the input signal of TIA attenuator pin. Single ended signal is converted to differential signals by differential amplifier. After passing through passive high pass filter, differential signals become bipolar. Finally, comparator circuit checks zero crossing after which it generates stop flag for the time to digital converter in processor module.

Spice simulations have been performed to verify differential signal amplification, bipolar pulse formation and comparator output. TIA output and differential amplifier outputs are shown in Figure A.7.

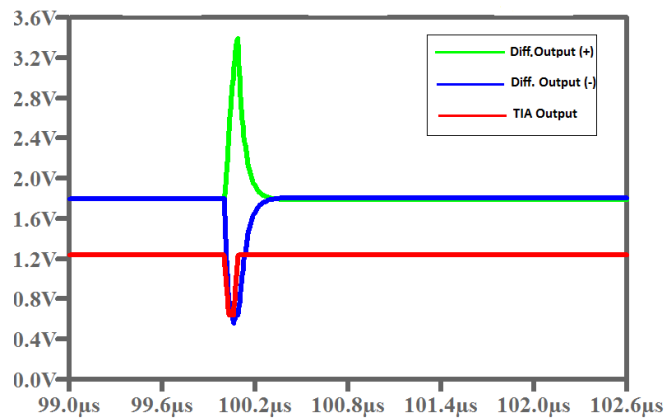


Figure A.7 TIA output and differential signal amplification

Bipolar pulse formation and stop flag signal is shown in Figure A.8.

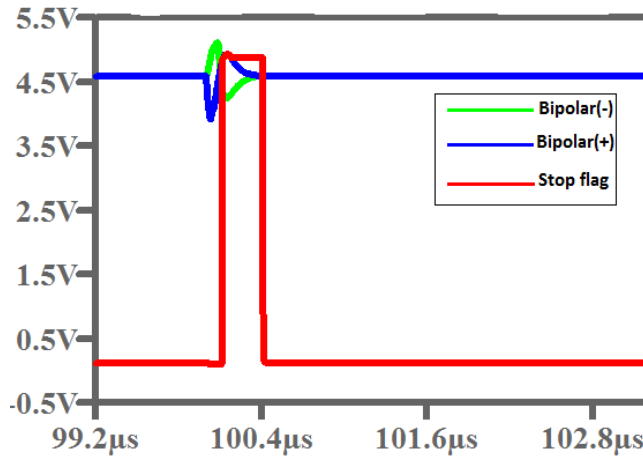


Figure A.8 Bipolar pulses and stop flag signal output

### Receiver PCB Layout

Receiver PCB layout is especially difficult due to high speed analog signal amplification. Parasitic inductance plays an important role to sample relatively true peak points. Otherwise, noise superimposed on the echo signal decreases measurement accuracy. Another important point is to eliminate any cross talk which affects receiver performance severely. Cross talk occurs when high speed signals are drawn very close to sensitive analog signals. Magnetic field created during high speed signal rise/fall time causes noises on signal paths drawn very close to itself.

Receiver PCB stack-up is the same as transmitter PCB. However, ground layer has been cut out just below the TIA input pins in order not to increase rise time. Parasitic capacitance affects signal rise times. 3D view of the receiver PCB is given in Figure A.9.

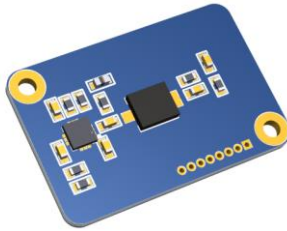


Figure A.9 3D view of receiver PCB

Each layer design is also shown in Figure A.10.

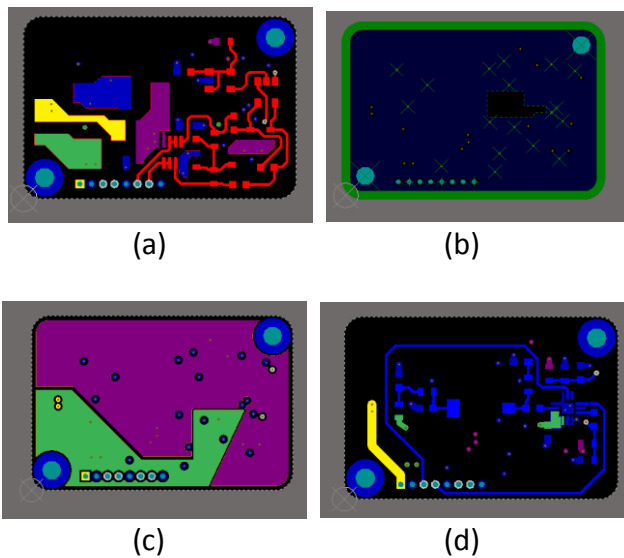


Figure A.10 (a) Signal (Top) Layer (b) Ground Layer (c) Power Layer (d) Signal (Bottom) Layer

### Processor Board

Processor board houses ARM microcontroller chip, TDC circuit, power supply circuit, full duplex RS485 interface and trigger interface. It is powered using 5VDC. STM32F407VGT6 from ARM Cortex M4 family was chosen as the processor to provide enough processing power required for measurement rate of at least 10000 per second [26]. The board has an interface with transmitter and receiver boards.

Start and stop flag signals are converted to CMOS compatible logic and monitored by TDC. TDC measures the time difference between these flags. Using SPI protocol TDC communicates with microcontroller and sends this time information to microcontroller. Microcontroller chip then calculates the range information. Trigger interface generates a 5V latched signal when the range is below a predetermined value.

**Time to Digital Converter**

TDC makes range calculations much easier assuming start and stop flags are generated accurately. Otherwise, measuring such short durations require more complicated electronics. TDC-GP22 from ACAM was used as TDC [27]. TDC circuit schematics is given in Figure A.11. As seen in the figure, TDC requires two crystals in order to measure time accurately. A clean power rail is also very important for TDC to operate properly.

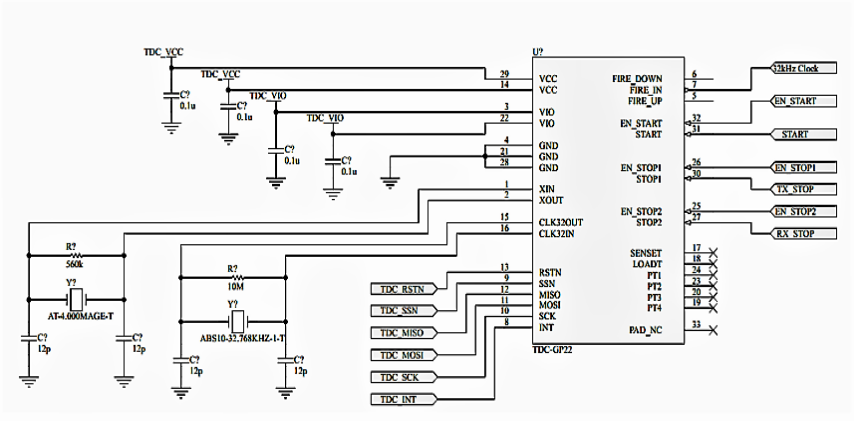


Figure A.11 TDC Circuit Schematics

## APPENDIX B

### SPLPL90 AND BP104FAS TECHNICAL SPECIFICATIONS

Table B.1 Technical Specifications of Pulsed Laser Diode SPL PL 90 @ 25°C, 100 nsec, 2 KHz [14]

<b>Peak Output Power (W)</b>	25
<b>Source Size (μm)</b>	200x2
<b>Operating Current (A)</b>	30
<b>Threshold Current (A)</b>	0.75
<b>Typical Wavelength (nm)</b>	905 ± 10
<b>Spectral Width (nm)</b>	7
<b>Max Duty Cycle (%)</b>	0.1
<b>Pulse Width (ns)</b>	≤100
<b>Beam Divergence(deg. FWHM)</b>	25x9
<b>Reverse Voltage (V)</b>	3
<b>Package</b>	TO56

Table B.2 Technical Specifications of PIN Photodetector BP 104 FAS [19]

<b>Photocurrent(μA)(V<sub>R</sub>=5V, E<sub>e</sub>=1mW/cm<sup>2</sup>)</b>	34(≥25)
<b>Wavelength of maximum sensitivity (nm)</b>	880
<b>Spectral range of sensitivity (nm)</b>	730-1100
<b>Radiant sensitive area (mm<sup>2</sup>)</b>	4.84

Table B.2 Technical Specifications of PIN Photodetector BP 104 FAS (cont'd)

<b>Dimensions of radiant sensitive area (mm)</b>	2.2 x 2.2
<b>Half angle (degree)</b>	±60
<b>Dark current (nA) (<math>V_R=10V</math>)</b>	2( $\leq 30$ )
<b>Spectral sensitivity of the chip (A/W) (<math>\lambda=870nm</math>)</b>	0.63
<b>Rise and fall time (ns) (<math>V_R=5V</math>)</b>	20
<b>Capacitance(pF) (<math>V_R=0V</math>, f=1 MHz, E=0)</b>	48
<b>Noise equivalent power (pW/Hz<sup>1/2</sup>) (<math>V_R=10V</math>, <math>\lambda=870nm</math>)</b>	0.040

## **APPENDIX C**

### **LPS SIMULINK MODEL**

A high level layout of the LPS simulink model which consists of pulse generation, receiver, amplifier, ADC and signal processing blocks is given in Figure C.1

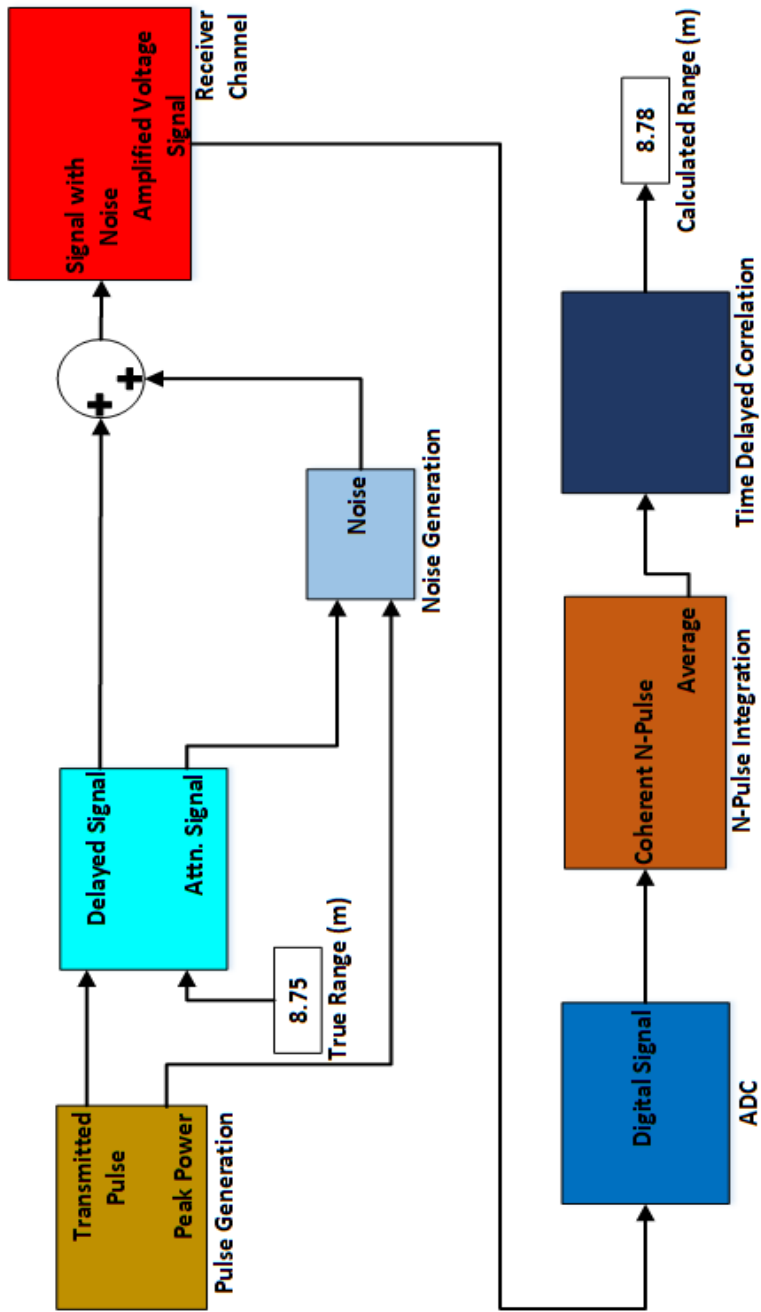


Figure C.1 The LPS Simulink Model Layout

## REFERENCES

- [1] R. D. Richmond S. C. Cain, *Direct Detection LADAR Systems*, SPIE Press, Washington, 8-23, 2009.
- [2] VK Arora, *Proximity Fuzes Theory and Techniques*, DRDO Monographs/Special Publications Series, New Delhi, 2010.
- [3] Velodyne LIDAR, Velodyne's HDL-64E: A High definition LIDAR sensor for 3D applications [White paper], 2007. Retrieved from [http://velodynelidar.com/docs/papers/HDL%20white%20paper\\_OCT2007\\_web.pdf](http://velodynelidar.com/docs/papers/HDL%20white%20paper_OCT2007_web.pdf) on date September 2017.
- [4] Velodyne LIDAR, Velodyne's HDL-64E. Retrieved from [http://velodynelidar.com/images/products/hdl-64e/HDL-64E\\_TopImage.png](http://velodynelidar.com/images/products/hdl-64e/HDL-64E_TopImage.png) on date September 2017.
- [5] M. C. Amann, T. Bosch, M. Lescure, R. Myllylä and M. Rioux, "Laser ranging: A critical review of usual techniques for distance measurement," *Opt. Eng.*, vol. 40, no. 1, pp. 10–19, 2001.
- [6] M. Buzinski, A. Levine and W. H. Stevenson, "Laser Triangulation Range Sensors: A Study of Performance Limitations," *Journal of Laser Applications* 4, 29, 1992.
- [7] M. D. McNeill, L. Williams, H. Chu, "Design of a Time of Flight Range-Finder," *29th IEEE Frontiers in Education Conference*, Nov 10-13, 1999.
- [8] G. Brooker, *Sensors and Signals*, University of Sydney, 2006.
- [9] W. Luhs, P5882 Laser Range Finder. Retrieved from <http://www.photonics.ld-didactic.com/images/XP-13Principle.jpg> on date

September 2017.

- [10] J. Brown, "Real-Time Hardware Design for Improving Laser Detection and Ranging Accuracy," The Florida State University, Tallahassee, FL, USA, 2012, *Int. J. Photoenergy*, vol. 2010, pp. 1–6, 2010.
- [11] P. Palojarvi, "Integrated Electronic and Optoelectronic Circuits and Devices for Pulsed Time-of-Flight Laser Range Finding," University of Oulu, Finland, 2003.
- [12] ZEMAX Optical Design Program, URL:<https://www.zemax.com>
- [13] Profile Basic Notes BN1000, "Laser Diodes", 2000. Retrieved from [http://michel.samsopagesperso-orange.fr/CoursMS\\_TS1/basic%20diode%20laser.pdf](http://michel.samsopagesperso-orange.fr/CoursMS_TS1/basic%20diode%20laser.pdf) on date September 2017.
- [14] OSRAM, Standard Pulsed Laser Diodes SPLPL90. Retrieved from [https://www.osram-os.com/Graphics/XPic0/00194565\\_0.pdf/SPL%20PL90.pdf](https://www.osram-os.com/Graphics/XPic0/00194565_0.pdf/SPL%20PL90.pdf) on date September 2017.
- [15] D. Hill, "The Relationship Between the FWHM and 1/e-Squared Halfwidth of a Gaussian Beam," 2007. Retrieved from <http://customers.zemax.com/os/resources/learn/knowledgebase/how-to-convert-fwhm-measurements-to-1-e-squared-ha> on date January 2017.
- [16] S. Thibault, "Astigmatic Light Source in Optical Design Software", *Opt. Eng.* 39(7), 1808-1811, Jul 01, 2000.
- [17] X. Lu, Z. Zhang, Y. Wang, L. Zhou, W. Chen, X. Gao, B. Bo, "Design of 980nm Semiconductor Laser Diode arrays and Optical Fiber Coupling System", *Optoelectronics and Microelectronics (ICOM)*, 2012 International Conference on, On page(s): 119 - 122.
- [18] THORLABS, LA1951-B - N-BK7 Plano-Convex Lens, Ø1", f = 25.4 mm,

- AR Coating: 650-1050 nm. Retrieved from <https://www.thorlabs.de/thorproduct.cfm?partnumber=LA1951-B> on date September 2017.
- [19] OSRAM, PIN Photodetector BP104FAS. Retrieved from [http://www.osram-os.com/Graphics/XPic4/00228994\\_0.pdf/BP%20104%20FAS.pdf](http://www.osram-os.com/Graphics/XPic4/00228994_0.pdf/BP%20104%20FAS.pdf) on date September 2017.
- [20] Z. Sun, J. Deng, “Pulsed laser ranging techniques based on digital signal processing methods for automobile anti-collision application,” *Proc. SPIE* 7160, 2008 International Conference on Optical Instruments and Technology: Optoelectronic Measurement Technology and Applications, 716023 (February 02, 2009).
- [21] OPENFILTERS Optical Interference Filter Design Software. Retrieved from <http://larfis.polymtl.ca/index.php/en/links/openfilters> on date July 2017.
- [22] MATLAB Simulink. URL: <https://www.mathworks.com/>
- [23] V. Delaye, P. Labeye, “High-resolution eye safe time of flight laser range finding”, *CEA-LETI*, France, 2000.
- [24] Laser Components, “Drive Electronics for Pulsed Laser Diodes - Power Where it Matters”. Retrieved from [https://www.lasercomponents.com/de/?embedded=1&file=fileadmin/user\\_upload/home/Datasheets/lc/applikationsreport/drive-electronics-pulsed-laser-diodes.pdf&no\\_cache=1](https://www.lasercomponents.com/de/?embedded=1&file=fileadmin/user_upload/home/Datasheets/lc/applikationsreport/drive-electronics-pulsed-laser-diodes.pdf&no_cache=1) on date October 2017.
- [25] Maxim Integrated, Receiver for Optical Distance Measurement MAX3806. Retrieved from <https://datasheets.maximintegrated.com/en/ds/MAX3806.pdf> on date September 2017.
- [26] STMicroelectronics, ARM Cortex-M4 168 MHz CPU STM32F407VGT6. Retrieved from <http://www.st.com/content/ccc/resource/technical/document/>

datasheet/ef/92/76/6d/bb/c2/4f/f7/DM00037051.pdf/files/DM00037051.pdf/jcr:content/translations/en.DM00037051.pdf on date September 2017.

- [27] ACAM Messelektronik GmbH, TDC-GP22 - Ultrasonic Flow Converter with integrated Analog Frontend. Retrieved from [http://www.acam.de/fileadmin/Download/pdf/TDC/English/DB\\_GP22\\_en.pdf](http://www.acam.de/fileadmin/Download/pdf/TDC/English/DB_GP22_en.pdf) on date September 2017.